JAMES | Journal of Advances in Modeling Earth Systems

RESEARCH ARTICLE
10.1029/2019MS001892

Special Section:
Presentation and analysis of the IPSL climate model used in CMIP6

LMDZ6A: The Atmospheric Component of the IPSL Climate Model With Improved and Better Tuned Physics

Frédéric Hourdin[1], Catherine Rio[2], Jean-Yves Grandpeix[1], Jean-Baptiste Madeleine[1], Frédérique Cheruy[1], Nicolas Rochetin[1], Arnaud Jam[1], Ionela Musat[1], Abderrahmane Idelkadi[1], Laurent Fairhead[1], Marie-Alice Foujols[1], Lidia Mellul[1], Abdoul-Khadre Traore[1], Jean-Louis Dufresne[1], Olivier Boucher[3], Marie-Pierre Lefebvre[2], Ehouarn Millour[1], Etienne Vignon[4], Jean Jouhaud[1], F. Bint Diallo[1], François Lott[1], Guillaume Gastineau[5], Arnaud Caubel[6], Yann Meurdesoif[6], and Josefine Ghattas[2]

[1]Laboratoire de Météorologie Dynamique/IPSL/Sorbone Universités/CNRS, UMR 8539, Paris, France, [2]CNRM, Université deToulouse, Météo-France, CNRS, Toulouse, France, [3]Institut Pierre Simon Laplace, IPSL/SU, Paris, France, [4]Environmental Remote Sensing Laboratory (LTE), École Polytechnique Fédérale de Lausanne (EPFL), Lausanne, Switzerland, [5]Locean/IPSL/Sorbone Universités/CNRS, Paris, France, [6]Laboratoire des Sciences du Climat et de l'Environnement, IPSL, unit mixte CEA-CNRS-UPS, Gif sur Yvette, Paris, France

Key Points:
- The development strategy of the LMDZ6A global atmospheric circulation model is presented
- Improvements with respect to previous versions are documented in the context of the Coupled Model Intercomparison Project, CMIP
- The improvements are based on significant changes of the physics content as well as on a better controlled tuning strategy

Correspondence to:
F. Hourdin,
frederic.hourdin@lmd.jussieu.fr

Citation:
Hourdin, F., Rio, C., Grandpeix, J.-Y., Madeleine, J.-B., Cheruy, F., Rochetin, N., et al. (2020). LMDZ6A: The atmospheric component of the IPSL climate model with improved and better tuned physics. *Journal of Advances in Modeling Earth Systems*, *12*, e2019MS001892. https://doi.org/10.1029/2019MS001892

Received 13 SEP 2019
Accepted 24 MAR 2020
Accepted article online 6 APR 2020

Abstract This study presents the version of the LMDZ global atmospheric model used as the atmospheric component of the Institut Pierre Simon Laplace coupled model (IPSL-CM6A-LR) to contribute to the 6th phase of the international Coupled Model Intercomparison Project (CMIP6). This LMDZ6A version includes original convective parameterizations that define the LMDZ "New Physics": a mass flux parameterization of the organized structures of the convective boundary layer, the "thermal plume model," and a parameterization of the cold pools created by reevaporation of convective rainfall. The vertical velocity associated with thermal plumes and gust fronts of cold pools are used to control the triggering and intensity of deep convection. Because of several shortcomings, the early version 5B of this New Physics was worse than the previous "Standard Physics" version 5A regarding several classical climate metrics. To overcome these deficiencies, version 6A includes new developments: a stochastic triggering of deep convection, a modification of the thermal plume model that allows the representation of stratocumulus and cumulus clouds in a unified framework, an improved parameterization of very stable boundary layers, and the modification of the gravity waves scheme targeting the quasi-biennal oscillation in the stratosphere. These improvements to the physical content and a more well-defined tuning strategy led to major improvements in the LMDZ6A version model climatology. Beyond the presentation of this particular model version and documentation of its climatology, the present paper underlines possible methodological pathways toward model improvement that can be shared across modeling groups.

Plain Language Summary The improvement of global numerical models is essential for the anticipation of future climate changes. We present significant advances in the physical content of a particular atmospheric model which contributes to the simulations of the Coupled Model Intercomparison project CMIP that feed reports from the IPCC. We document in particular the improvements of the representation through "parameterizations" of convective and cloudy processes. The article emphasizes the importance of strengthening the formalization of the methodology of development and tuning of models, so that new physical ideas can be translated into effective improvement of the climate representation.

1. Introduction

It is commonly accepted that a large part of the uncertainty in future climate change projections with global climate models comes from the representation of unresolved physical processes through so-called parameterizations, and in particular from the parameterizations of turbulence, convection, and clouds. The same parameterizations are also responsible for large errors, which persist in the representation of present-day climate with global models.

There are a lot of steps between the idea for a new parameterization and the demonstration of associated robust improvements in a climate model. Because of this, alternative approaches to parameterizations have been developed such as embedding reduced "large eddy" resolving models in each column of a global model (Khairoutdinov et al., 2005; Kooperman et al., 2016; Li et al., 2012; Stan et al., 2010) or training deep learning algorithm against large eddy simulations (LES) (Gentine et al., 2018) in order to break the so-called parameterization deadlock (Randall et al., 2003). In the meantime several limitations of traditional convection schemes have been overcome by developments of new concepts and ideas for the parameterization of convection and clouds (Rio et al., 2019) that are starting to find their way into climate models. New convective parameterizations are developed more and more by targeting LES results: New approaches are often inspired by analyzing LES before tuning and assessing the proposed parameterizations by comparing single-column model (SCM) simulations with LES results using the exactly same setup. The difficulty of going from a new idea to a robust improvement in large-scale models has several fundamental origins: (1) The requirements put on parameterizations are large. They should be able to represent the particular process for one or a few setups, but they should also behave well in all the climate regimes encountered from the equator to the poles, or ocean to continental conditions, representing not only the meteorology but also the transport of trace species; (2) the numerical implementation should be robust and fast enough to compute hundreds of years of climate on, typically, 10^4 to 10^6 atmospheric "columns" with a typical time step of a few tens of minutes. Thus, compromises have to be made between robustness and complexity, between time resolution and accuracy; (3) whatever their complexity and accuracy, parameterizations are an idealized and approximate representation of processes that depend on "free parameters," which are often not observable per se and require adjustment or tuning (Hourdin et al., 2017; Schmidt et al., 2017). In particular, no parameterization of convection and clouds (even LES) is able to simulate the radiative effect of clouds from first principles and well-constrained parameters to an accuracy which is better than 10 W/m^2, while a change of 1 W/m^2 for the global radiative budget at the top-of-atmosphere typically results in a change of 1 K in global surface temperature in a coupled ocean atmosphere model. A 1 K departure from the observations for the global mean temperature is typically the maximum value encountered in simulations of the present-day climate available from the Coupled Model Intercomparison Project (CMIP, Taylor et al., 2012), meaning that all CMIP class models are tuned in one way or another.

We present a summary of changes that have been achieved over the last 15 years in that direction with the LMDZ model, the 6A version of which constitutes the atmospheric component of the IPSL-CM6A coupled model used for the 6th phase of CMIP. An important aspect of this paper is to promote an object-oriented framework for the parameterization of convection. While many authors advocate the development of unified parameterizations for convection (e.g., Arakawa & Wu, 2013; Park, 2014), the deliberate choice was made to use distinct parameterizations for the following:

- small scale turbulence;
- boundary layer convection (unified between dry and cloudy);
- deep convection associated with cumulonimbus; and
- cold pools created below cumulonimbus by reevaporation of convective rainfall.

In this approach, the life cycle of convection is controlled by the interplay between the various objects. Their coupling itself therefore requires to be parameterized. During the morning over continents, dry and shallow convection controls deep convection preconditioning and triggering, while the horizontal spread of cold pools at the surface initiates new convective columns that maintain convection until the early night. This approach also favors the possibility for different regimes to coexist within the same model column. The major success of this approach is a better representation of shallow cumulus (Jam et al., 2013) over tropical oceans in particular, and a shift by several hours of the maximum rainfall over tropical continents, in better agreement with observations (Rio et al., 2009), solving one of the major problems underlined by Randall et al. (2003).

The first LMDZ version based on this "New Physics" (NP) called LMDZ5B (Hourdin et al., 2013) was used to perform a subset of the simulations for CMIP5 (Dufresne et al., 2013). It was also the first version of the LMDZ model to benefit from parameterizations inspired and assessed with LES. Because of several parameterization shortcomings and because of an insufficient maturity and tuning of the 5B version, and despite the aforementioned improvements, this version was significantly worse than the 5A "Standard Physics" version in terms of classical metrics used to assess CMIP simulations concerning the representation of the large-scale

atmospheric circulation. Some of the explanations for this disappointing behavior were understood afterward and motivated new model improvements as well as the definition of a more systematic methodology for model configuration, tuning, and assessment.

The 6A version of LMDZ is built upon 5B with significant modifications concerning the following:

- the introduction of a stochastic triggering designed to make the frequency of occurrence of new convective systems within a grid cell aware of the grid cell size (Rochetin et al., 2014a, 2014b);
- a modification of the shallow convection scheme, the so-called "thermal plume model," to account for stratocumulus clouds (Hourdin et al., 2019);
- the introduction of the latent heat release associated with water freezing (not accounted for until now);
- a new parameterization of nonorographic gravity waves targeting the representation of the quasi-biennial oscillation (QBO);
- a careful tuning of boundary layer turbulence in very stable conditions (Vignon et al., 2018); and
- a significant refinement of the vertical grid, both for the QBO issue and for a better representation of boundary layer clouds.

The present paper aims to be the reference paper for LMDZ6A. It explains the development strategy, describes the model content and targets of the model tuning, and documents the impact on dominant aspects of the climate system representation. A companion paper has been recently published on changes in boundary layer clouds and associated cloud radiative forcing in the same model version (Hourdin et al., 2019). Another paper focuses on the coupling with continental surfaces (Cheruy et al., 2019MS002005, submitted to the same Special Collection). The analysis presented here mainly focuses on aspects that are not covered by those two companion papers and focuses more specifically on the radiative tuning and evaluation, mean atmospheric state, and rainfall space time distribution. It is based on stand-alone atmospheric simulations forced by observed sea surface temperature (SST). The horizontal resolution used for CMIP6 is rather coarse, but we also document simulations performed with a much finer grid of 50 km for the HighResMIP part of CMIP6. Comparison of these low- and high-resolution versions allows us to distinguish the part of the model biases linked to the coarse resolution from that which is more fundamentally related to the model physical content.

The paper also underlines the strategy followed for this model development and tuning which, although still not optimum, resulted in significant and robust improvements in many aspects of the model climatology without degrading other aspects too much.

Section 2 is dedicated to the description of the model, focusing on the improvements and additions with respect to previous versions. Section 3 documents and comments on the major changes in the mean model climatology compared to the previous versions. Section 4 is dedicated to the representation of convective rainfall and monsoon. Section 5 concludes on robust success, both in terms of model improvements and methodologies. It also presents remaining shortcomings and directions for future research.

2. Development of the LMDZ "New Physics"

2.1. The LMDZ Model From its Origins to Version 5A

The LMDZ general circulation model comes from a rewriting of a former version of the LMD model developed by Sadourny and Laval (1984) and Laval et al. (1981) in the 1980s. The dynamical core is based on a finite difference discretization of the primitive equations of meteorology on an Arakawa C grid (Kasahara, 1977), favoring the conservation of enstrophy rather than that of energy following ideas from Sadourny (1975). It uses a longitude-latitude grid on the horizontal, with the possibility of refining the grid in both longitude and latitude (the Z in LMDZ coming from this zoom capability), and a classical hybrid σ-pressure terrain following coordinate on the vertical. To avoid using very small time steps that would be required by CFL criteria when the longitudinal horizontal step tends to zero at the pole, a longitudinal filter is used close to the pole. This limits the efficiency of domain decomposition for parallelism in longitude. The current version of the dynamical core is thus parallelized in latitude, with distributed memory using MPI, and on the vertical with shared memory using OpenMP.

The coupling between dynamics and physical parameterizations is done through a generic interface, making full use of the fundamental 1-D nature of physical parameterizations that only compute vertical transfers.This interface makes LMDZ a flexible tool. In particular, the same dynamical core is used for planetary

atmospheres of the solar system like Mars (Wang et al., 2018), Venus (Navarro et al., 2018), Titan (Lebonnois et al., 2012) or Pluto (Bertrand & Forget, 2016), and for extrasolar planets (Turbet et al., 2018). The exact same source files can be used in 1-D mode for physics developments, or in 3-D climate mode, forced by SST or coupled to an external oceanic model (Nemo for the IPSL coupled model Madec et al., 2017) or to a slab ocean (available within LMDZ source files Codron, 2012; L'Hévéder et al., 2015), coupled to an external model of the continental surface (Orchidee model in general D'Orgeval et al., 2008) or coupled to an idealized bucket version or a version with imposed ratio of evaporation to potential evaporation (Coindreau et al., 2007). It can also be used in aquaplanet (with imposed SST that depends on latitude only) or terraplanet (like a global desert) mode, or be nudged by reanalyzed fields to force the model to follow the observed day-to-day synoptic situation (see, e. g., Diallo et al., 2017). The 1-D nature of the physical parameterizations also enables a more efficient parallelism than for the dynamical core by splitting a single vector that runs through the entire horizontal grid into independent domains, which are managed in shared memory with a combination of MPI and OpenMP process.

One of the main applications of the terrestrial version of LMDZ is as the atmospheric component of the IPSL coupled model, and the participation with this coupled model to the CMIP exercises. Each of these exercises, which are separated by about 7 years, is the occasion to derive new reference configurations of the model, which consist in (1) choosing a new grid configuration, (2) improving the physics content of the model, and (3) tuning the model free parameters. The LMDZ model first participated in CMIP phase 3, associated with the fourth IPCC assessment report. The LMDZ4 version used for CMIP3 is described in Hourdin et al. (2006). It was kept almost unchanged for CMIP5 and was labeled as the 5A versions (Hourdin et al., 2013) of LMDZ and IPSL-CM.

In the 4 and 5A versions, the Morcrette (1991) scheme is used for radiative transfer. Drag and lifting effects associated with the subgrid-scale orography are accounted for according to Lott (1999). Turbulent transport in the planetary boundary layer is treated as a vertical diffusion with an eddy diffusivity K_z depending on the local Richardson number according to Laval et al. (1981). Up-gradient transport of heat in the convective boundary layer is ensured by adding a prescribed counter-gradient term of 1 K/km to the vertical derivative of potential temperature (Deardorff, 1966). In the case of unstable profiles, a dry convective adjustment is applied. The surface boundary layer is treated according to (Louis, 1979). Deep convection is parameterized using the "episodic mixing and buoyancy sorting" Emanuel scheme (Emanuel, 1991) which assumes quasi-equilibrium between the large-scale forcing of convection and convective instability.

For the representation of clouds, statistical scheme is used, based on the specification of a probability distribution function (PDF) for the subgrid-scale distribution of total water (q_t). Given this distribution, the cloud fraction within a grid cell and cloud condensate content are $\int_{q_{sat}}^{\infty} PDF(q_t)\mathrm{d}q_t$ and $\int_{q_{sat}}^{\infty}(q-q_{sat})\,PDF(q_t)\mathrm{d}q_t$, respectively, where q_{sat} is the specific humidity at saturation. For deep convection, condensation and rainfall are computed directly by the Emanuel convective scheme so that the statistical cloud scheme is used for radiation only. In this case, a log-normal PDF is computed following Bony and Emanuel (2001) so as to match the in-cloud condensed water predicted by the convective scheme. All other clouds are handled by a so-called "large-scale condensation scheme." The scheme computes the cloud fraction and the condensate content downward from the top of the atmosphere using the statistical cloud scheme. The width of the PDF is imposed as a function of pressure $r(p)$ times the total water in the grid cell $\sigma = r(p)q_t$. Once the in-cloud condensed water is computed, a fraction of it is converted into precipitation. Part of this precipitation is reevaporated in the lower layer, before applying the statistical scheme, and continuing the calculation iteratively, down to the ground surface.

We describe below the main modifications done when introducing the New Physics package, leading to a first version 5B used for CMIP5, and then the improvements from this 5B version to the most recent 6A version of this New Physics.

2.2. Development of the 5B Version

The change from the 5A to the 5B version corresponds to a complete rethinking of the parameterizations of turbulence, convection, and clouds and was the result of intense research (Hourdin et al., 2013).

First, in the 5B version, the computation of eddy diffusion was improved by introducing a prognostic turbulent kinetic energy (TKE) according to Yamada (1983). The turbulent mixing coefficient K for momentum

(subscript "m") and for heat or vapor (subscript "h") now reads:

$$K_{m,h} = lS_{m,h}\sqrt{2\mathrm{TKE}} \quad (1)$$

where l is the mixing length and $S_{m,h}$ are semiempirical stability functions of the Richardson number.

More importantly, a mass flux parameterization of the organized structures of the boundary layer was introduced in lieu of the countergradient term and the dry adjustment (A dry convective adjustment is still activated above the thermal plumes). The idea of combining a mass flux scheme for boundary layer convection with an eddy diffusion parameterization to represent vertical transport in the convective boundary layer traces back to a proposition by Chatfield and Brost (1987) and is since, often referred to as the Eddy Diffusion Mass Flux (EDMF) approach. The "thermal plume model" developed for LMDZ was the first EDMF scheme ever tested in a climate model (Hourdin et al., 2002). The cumulus clouds associated with the upper part of thermal plumes are predicted by using a bimodal distribution of subgrid-scale water (Jam et al., 2013) instead of a single-mode PDF, one Gaussian mode being associated with the fraction of the grid covered by rising plumes and the other mode representing their environment using a log-normal distribution. To better account for the possible correlations of total water and temperature, this PDF is prescribed as a function of the deficit at saturation s (difference between the total specific humidity and that at saturation) rather than total specific humidity q_t, so that the cloud fraction within a grid cell and cloud condensate content read $\int_0^\infty PDF(s)\mathrm{d}s$ and $\int_0^\infty s\ PDF(s)\mathrm{d}s$, respectively. The mass flux scheme directly provides the mean value of the two modes, as the bulk value of s within the plume and within the environment of the plumes. The parametrization of the width of the distributions is described by Jam et al. (2013). The computation of associated clouds is done directly in the large-scale condensation scheme described above. For grid cells not affected by the thermal plume parameterization, only one log-normal is used, which width is a function of pressure as in the 5A version, $\sigma = r(p)s$.

With these changes, the 5B version produced more cumulus clouds, in better agreement with observation.

The 5B version also includes for the first time a parameterization of the cold pools (density currents or wakes) created below cumulonimbus by evaporation of convective rainfall (Grandpeix & Lafore, 2010; Grandpeix et al., 2010). Each grid cell is assumed to contain a part of a population of cold pools randomly distributed horizontally with a prescribed number density per unit area. The ensemble of cold pools is represented by a mean cold pool described by additional internal state variables: the fraction of the surface covered by the cold pool and the differences between the cold pool and its environment for temperature and moisture. The shape of vertical velocity difference is specified as some idealized profile. The fraction covered by cold pools can grow up to 0.4. The horizontal spreading of the negatively buoyant cold pools creates upward motions at their boundary that are used to generate new convective cells.

The third important change in the 5B version concerns the triggering and the closure of the deep convective scheme. The parameterization of deep convection uses a modified version (Grandpeix et al., 2004) of the Emanuel's scheme (Emanuel, 1991). It consists in a mass flux approach in which a buoyancy sorting is used to estimate mixing between the adiabatic ascent and the environment in the bulk cumulonimbus cloud. In version 5A, the Emanuel's scheme is activated—or "triggered"—only if the buoyancy of the lifted parcel is positive at 40 hPa above cloud base level (Lifting Condensation Level, LCL). Once triggered, the cloud base mass flux is a function of the total amount of instability in the free troposphere (Convective Available Potential Energy, or CAPE). Concerning deep convection intensity, we have then here a typical "CAPE-based closure."

In the 5B version, this closure was entirely revisited (Rio et al., 2013). First, the triggering criterion assumes a kinetic energy provided by the subcloud processes, such as thermal plumes and density currents, likely to lift the parcel up to its level of free convection (LFC). The so-called available lifting energy, or ALE, must then exceed the convective inhibition (CIN) typically met at the top of the PBL to trigger a deep cloud in the grid. Second, the closure hypothesis now relies on an available lifting power, or ALP, delivered by these subcloud processes, which directly controls the cloud base mass flux. ALP is the flux of kinetic energy through the bulk cloud base cross section. It scales with the power 3 of the vertical velocity related to the thermal plumes and wakes.

In this approach, the boundary layer convection, deep convection, and cold pools interplay without being as strongly tied as they used to be to the large-scale forcing. The boundary layer controls the appearance

and growth of the first cumulus clouds, then a large cumulus can initiate deep convection, which will then create cold pools that can initiate new convection. This new set of parameterizations resulted in a significant improvement to the diurnal cycle of rainfall over continents, with a time shift of several hours in the afternoon, while rainfall was peaking at noon, in phase with solar forcing, in the former version (Rio et al., 2009).

Despite those significant improvements in the physics content and representation of some key processes, the 5B version was generally worse than the 5A version for metrics related to the representation of the atmospheric general circulation. Several shortcomings were identified (at the time or since then) that explain these deficiencies, and overall it can be seen as a lack of maturity of this model version, that is, our lack of expertise regarding the aforementioned numerous and significant changes included into the physics at the time of the CMIP5 exercise.

2.3. Identified Shortcomings of the 5B Version

One of the identified shortcomings was the tendency of the model version to trigger deep convection too often in the tropics. Indeed, in the 5B version, convection was triggered as soon as the ALE associated with the maximum vertical velocity in the thermal plume was overcoming the convective inhibition. The deep convective scheme was activated for all active cumulus (i.e., showing an acceleration above cloud base), including clouds that did not reach the freezing level (typically "mediocris" cumulus type in meteorology) and thus did not create significant surface rainfall. The subsequent activation of the deep convection parameterization was in part canceling the improvement on low cloud fraction coming from the introduction of the thermal plume and bimodal statistical cloud scheme, which were calibrated for such cases (Jam et al., 2013).

The 5B version was also displaying a stronger rainfall variability in the tropics, compared to a very weak variability in the former 5A version. This increased variability was partly due to an improvement of the representation of the sensitivity of deep convection to tropospheric humidity via entrainment (Grandpeix et al., 2004). However, rainfall variability in the 5B version was too strong and was also partly due to grid point storms created by the large-scale condensation scheme, compensating for a weaker activity of the deep convection scheme.

Another shortcoming is related to stratocumulus clouds. As will be explained below, a trick was introduced to deactivate thermal plumes under strong inversion. The trick was successful in maintaining in regions were stratocumulus are expected, banks of clouds which were otherwise disappearing. However, the base of the resulting stratocumulus was located too close to the surface, resulting in an overestimation of the long-wave radiation reaching the surface. This additional surface warming was in fact overcompensating the cooling associated with the additional shadowing effect of clouds. Moreover, because the mass flux transport was deactivated, the near-surface relative humidity was overestimated, thereby reducing the surface evaporative cooling. Because of these two effects, the surface cooling was globally underestimated in the version 5B. This contributed to increase rather than reduce the classical warm biases on the west side of tropical oceans in coupled atmosphere-ocean simulations (Hourdin et al., 2015).

Also, this first version of the thermal plume model was not very stable numerically, even with a rather short physics time step of 7.5 min. This also significantly altered the representation of low clouds. Finally, the tuning of the radiative effect of clouds in this version was not pushed far enough. As a consequence, the latitudinal distribution of cloud radiative forcing was, for instance, not well represented. Related to this tuning or not, the midlatitude jets, which were already too close to the equator in the 5A versions, were even closer to the equator in the 5B version.

These shortcomings drove, for a large part, the new developments and adjustments that define the LMDZ6A version described below.

3. The LMDZ6A Physics

3.1. Small-Scale Turbulence

The representation of small-scale turbulence, based on a Yamada (1983) 1.5 order closure eddy diffusion scheme, was modified in several aspects compared to version 5B.

Following the recommendations of, for example, Holtslag et al. (2013) and Sandu et al. (2013), particular attention was paid to the representation of very stable boundary layers that occur, for instance, over the

ice sheet plateaus and boreal lands in winter. Such boundary layers can experience very weak and intermittent turbulence even close to the ground surface, pushing the current state-of-the-art subgrid mixing parametrizations and underlying physical assumptions to their limits and even beyond. The Yamada (1983) scheme was thus revisited in this context. First of all, the minimum threshold value of 1 m prescribed for l was removed. Initially set in LMDZ5 to maintain some mixing in stable conditions over continents, this threshold value was also shown to help the numerical convergence of the TKE equation, impeding an artificial cut-off of the turbulence even at moderate stability when using standard time step values (Vignon, 2017). This trick was responsible for an excessive vertical mixing. It was removed thanks to a new numerical treatment of the TKE equation making the trick useless. The reduction of the lower-bound values for $S_{m,h}$ set in Yamada (1983) also helped reduce mixing in very stable conditions (Vignon et al., 2017).

3.2. Boundary Layer Convection

As in the 5B version, the boundary layer convection is represented with the thermal plume model (Hourdin et al., 2002; Jam et al., 2013) with two major improvements. The first improvement concerns the numerical stability, which was improved by using a time implicit scheme and upwind space finite volume scheme to compute the downward transport in the environment of the plume. The effect of this change is documented in the next section. The second improvement concerns the representation of stratocumulus clouds. As explained above, the thermal plume model was deactivated in the region of strong subsidence in version 5B because it was dissipating stratocumulus clouds due to a too strong entrainment of dry air from the free troposphere at the inversion level. In order to prevent the scheme from entraining too much air from the dry troposphere into the stratocumulus layers, the buoyancy B used in the parameterization lateral detrainment from the plume (detrainment is strong when the buoyancy is negative) was modified by using the contrast between the virtual potential temperature in the updraft $\theta_{v,up}(z)$ at level z and the virtual potential temperature in the environment at a higher altitude $z^* = z + \lambda_d \times z$: $B = g[\theta_{v,up}(z) - \theta_v(z^*)]/\theta_v(z)$. The value of the λ_d parameter was fixed to 0.07 in the 6A version. With this simple modification proposed by Jam (2012), the buoyancy starts to become strongly negative before reaching the inversion level, inducing a stronger detrainment there. The thermal plume is therefore stopped earlier with the modified formulation. The upward plume transport at the inversion is thus reduced, and the top entrainment of dry tropospheric air (responsible for dilution of the stratocumulus in the absence of modification) by the compensatory mass flux is reduced accordingly. The modified thermal plume model represents both the cumulus and stratocumulus clouds reasonably well, in a unified manner, that is, without switching from one scheme to another (Hourdin et al., 2019). Due to this modification, the simulated downward surface fluxes are reduced in the region of stratocumulus because of a reduced greenhouse effect and enhanced evaporative cooling compared to version 5B. This reduced downward flux reduces in turn the warm bias in coupled simulations (Hourdin et al., 2019). In addition to those two major changes of the scheme itself, the large-scale environment provided to the thermal plume model is the off-cold pool environment instead of the mean column profile. With this change, the thermal plume "sees" vertical profiles that are more unstable, which in turn reinforces the thermal plumes intensity giving more weight to the shallow convection when shallow and deep convection coexist.

3.3. Deep Convection

As in the 5B version, the representation of deep convection is based on the Emanuel mass flux scheme with an ALE-triggering and ALP-closure. Compared to the 5B version described by Rio et al. (2013), triggering by boundary layer thermals was revisited in the 6A version.

We now assume a coupling between shallow and deep convection at the cumulus base level. Therefore, the lifting energy ALE_{BL} provided by thermal plumes (see Section 2.2) is computed with an estimate of a maximum vertical velocity at the LCL instead of a maximum velocity in the whole subcloud layer. In addition, we introduce an exponential distribution for the cloud base cross sections, deduced from the mean thermal plume properties computed by the mass flux scheme. For each cloud, we also suppose a Gaussian distribution for the vertical velocities of the drafts crossing the cumulus base. Assuming independent drafts in the cloud and independent clouds in the domain makes it possible to combine these two probability distribution functions (PDF) and get a statistical estimate of the maximum vertical velocity at LCL, from which ALE_{BL} can finally be deduced and compared to the CIN. If ALE_{BL} exceeds the CIN, triggering may happen. More importantly, another criterion is required to trigger deep convection: The cloud population must host at least one cumulus whose cross-section at LCL is larger than a prescribed threshold S_{Trig}. In other

words, when the fastest thermal of the domain crosses the inhibition layer, the associated cumulus must be wide enough to protect its core from dry air intrusions through lateral entrainment in order to maintain its positive buoyancy and to then have a chance to turn into a congestus or a cumulonimbus. This is where the stochastic nature of the new triggering scheme comes in. A nontriggering probability P is computed by comparing an estimated cloud base cross-section PDF (see details in Rochetin et al., 2014a) to the threshold cross-section S_{Trig} and compared to a random sampling R: If $R > P$ then the Emanuel's scheme is activated. This stochastic component emphasizes the episodic and intermittent nature of deep convection usually met under semiarid or semihumid climates. Moreover, for a given simulated cloud scene, this scheme is scale aware: It gives statistically (i.e., for a reasonable number of realizations) the same number of triggerings per unit area regardless of the grid spacing used. The closure is finally modified to ensure consistency with the new triggering. Since the triggering probability P' ($P' = 1 - P$) ultimately scales a cumulonimbus spatial density, the lifting power delivered by thermals (ALP_{BL}) must simply be scaled by the inverse of the triggering probability P' to get a consistent cloud base mass flux.

3.4. Representation of Clouds

A detailed description of the cloud scheme used in the version 6A of LMDZ can be found in Madeleine et al. (this Special Collection, manuscript 2020MS002046).

As in the 5A and 5B version, the cloud associated with the deep convection are computed using a log-normal PDF of total water following Bony and Emanuel (2001). As in version 5B, all the other clouds are computed by the large-scale condensation scheme described above, using a single-mode or bimodal distribution of the deficit at saturation. Note that in this approach, the shallow cumulus clouds are thus parameterized by combining the thermal plume model for transport and the large-scale condensation scheme for clouds. Liquid water and ice are bulk variables in LMDZ, that is, only the moist-air mass mixing ratio as well as liquid water and ice mass mixing ratios are predicted by the cloud scheme. Cloud droplet and crystal number concentrations are diagnosed afterward for the radiation scheme only (as explained in the following sections).

The phase partitioning in cold clouds is based on an analytical function that gives the fraction of supercooled liquid droplets as a function of temperature. Supersaturation with respect to ice is not represented in the model, although work is underway to parameterize this process. At subfreezing temperature, the amount of condensed water vapor is simply based on the saturation vapor pressure with respect to ice. Once the in-cloud condensed water is computed, a fraction of it is converted to rain or snow and can be reevaporated in layers below. When formed at subfreezing temperatures, rain freezes and is converted to snow.

From the 5B version to the 6A version, efforts were made to improve four main processes. (1) Rain reevaporation in a given atmospheric layer was limited by the saturation of a fraction of the horizontal grid cell equal to the cloud fraction in the layer just above. This cloud fraction is now replaced by the maximum cloud fraction found in the overlying contiguous cloud layers. (2) The function of temperature used to compute the fraction of supercooled liquid droplets has been updated to be more consistent with the latest satellite observations. Supercooled liquid water was assumed to exist down to a temperature of −15 °C in the 5B version. This temperature was changed to −30 °C in LMDZ6A. 3) As explained above, the shallow convection scheme was improved to better predict stratocumulus clouds (Hourdin et al., 2019). 4) The latent heat exchanges due to the melting of ice or freezing of droplets, which were neglected in LMDZ5 (the same latent heat was used so far for vapor-liquid and vapor-ice transformations), were introduced in both the large-scale cloud scheme and deep convection scheme. Related to this change, a bug was fixed in the computation of humidity at saturation, and an iterative scheme was introduced for the computation of this humidity at saturation to account for the adjustment of condensation and temperature. A first attempt was also made to introduce a subgrid-scale distribution to account for vertical heterogeneities of clouds within a layer, based on a preliminary version of the work by Jouhaud et al. (2018). However, the values of the associated free parameters were adjusted in a way that the parameterization does not significantly modify the distribution of clouds.

3.5. Representation of Aerosols and Aerosol-Cloud Interactions

Tropospheric aerosols are imposed as climatological 3-D distributions of sulfates, nitrates, organic carbon, black carbon, dust, and sea salt mass mixing ratios. The climatologies vary monthly and annually as computed in a previous simulation of the LMDZORINCA model using a quasi-final configuration of the LMDZ6 model and CMIP6 emissions of aerosols and aerosol precursors, except for dimethylsulfide (DMS), sea salt

and dust aerosols whose emissions are generated interactively in the model. The CMIP6 monthly emissions were interpolated to daily values with a correction term to conserve the monthly mean (Lurton et al., 2020). The monthly climatologies are interpolated at the daily timestep assuming that the monthly mean represents the mid-month value.

Stratospheric aerosols were provided by CMIP6 as a two-dimensional (latitude-height) climatology of the aerosol extinction coefficient, single-scattering albedo, and asymmetry parameter (Thomason et al., 2018) averaged over each of the wavebands of the model radiative code. The climatology varies monthly and annually and is regridded to the model resolution (in latitude and altitude) with values below the diagnosed model tropopause being masked (Lurton et al., 2020). Both the direct and first indirect effect of aerosols are considered in LMDZ6. The optical properties for tropospheric aerosols were recomputed using Mie theory for the new wavebands of the radiation code assuming an external mixture and considering spectrally varying refractive indices (Lurton et al., 2020). It should be noted that only dust and stratospheric aerosols interact with long-wave (LW) radiation.

The first indirect effect is restricted to liquid clouds and to the liquid fraction of mixed clouds. In other words, ice cloud properties do not depend on aerosol properties and concentrations. The cloud droplet number concentration (CDNC) is computed from the sum of accumulation mode soluble aerosols with a modified empirical law following (Boucher & Lohmann, 1995). The parameters of this empirical law have been slightly adjusted during the tuning process, thus impacting the aerosol effective radiative forcing (ERF). It should be noted that CDNC is bound between 10 and 1,000 cm^{-3}. The effective cloud droplet radius is computed from the cloud liquid water content and the CDNC, with a minimum value of 5 μm. The optical properties of liquid clouds as a function of effective cloud droplet radius and liquid water content are those of the radiative scheme as they were implemented in the ECMWF model.

The ERF for tropospheric aerosols was estimated to be −0.62 W m^{-2} from fixed-SST experiments for present-day (2014) relative to preindustrial (1850) conditions. The contribution of aerosol-radiation interactions is slightly higher than that of aerosol-cloud interactions as estimated from double radiation calls, with values of −0.38 and −0.34 W m^{-2}, respectively, for a total instantaneous radiative forcing of −0.73 W m^{-2} (Lurton et al., 2020).

Finally, it should be noted that aerosols do not modify the precipitation efficiency. This is a deliberate choice given the large uncertainties associated with the relevant microphysical processes.

3.6. Radiation

The radiative codes in LMDZ are inherited from the ECMWF weather forecast model.

Compared to versions 5A and 5B, the broadband flux emissivity method used in the thermal infrared (Morcrette, 1991) was replaced by the RRTM code (Mlawer et al., 1997) based on a *k*-correlated scheme with 16 spectral bands. The improvement due to the change of infrared radiative code can reach 10 W m^{-2} for longwave radiation, as illustrated, for instance, in Figure 3 of Vignon et al. (2018) over the Antarctic Plateau.

The shortwave part of the computation was updated with the number of spectral intervals increased from two to six in order to better distinguish near-infrared, visible, and ultraviolet radiation. The gaseous active species are H_2O, O_3, CO_2, N_2O, CH_4, and chlorofluorocarbons and other halocarbons (lumped together as equivalent mixing ratios of CFC11 and CFC12).

Albedo for the open surface ocean is computed at every time step and for each waveband as a function of solar zenith angle and surface wind speed following Séférian et al. (2018), which brings a significant improvement in the parametrization used in the LMDZ5 model.

The effective radius of cloud droplets depends on aerosol concentration as explained above (first indirect effect). The effective size of ice crystals is imposed directly as a function of the ambient temperature using a formula proposed by Iacobellis and Somerville (2000) with an asymptotical value of 3.5 μm at $T < -81.4$ °C added to be consistent with observations by Heymsfield (1986). This parametrization is unchanged compared to LMDZ5, but the optical properties of ice clouds as a function of effective crystal size are those of the RRTM scheme as implemented in the ECMWF model.

3.7. Surface Layer and Coupling

Between the 5A or 5B version and the 6A version of the IPSL model, the Orchidee land surface model was deeply revisited as well. In particular, the old 1.5-layer model for hydrology was replaced by a fully discretized scheme. These changes and their impact on the coupling with continental surfaces will be fully described in a companion paper (Cheruy et al., 2019MS002005, submitted to the same Special Collection).

Several modifications were made in the representation of the surface layer of LMDZ as well. First, and consistently with the changes done in the boundary layer to allow strong decoupling in stable atmospheres, the so-called "long-tail" stability functions from Louis et al. (1982) that artificially enhance the surface turbulent fluxes in stable conditions were replaced by more realistic "short-tail" functions from King et al. (2001). This was shown to strongly improve the representation of surface temperature on the very flat ice sheet of the Antarctic plateau. For rugged surfaces, an additional term was introduced in the TKE equation and was computed from the drag of subgrid-scale orography. This modification has not been fully analyzed yet but has a second-order effect on the results.

A second important change concerns the computation of surface roughness height z_0. While a single value was used in former versions for all model state variables, different values are now used for horizontal momentum $z_{0,m}$, thermodynamical variables $z_{0,h}$, and tracers $z_{0,q}$. Over the ocean, a parameterization of the gusts generated by thermal plumes and wakes was introduced to reinforce surface fluxes in condition of weak winds. The gustiness is computed directly as a combination of the ALE with coefficients that were adjusted to reproduce results similar to the analysis of the Toga-Coare campaign by Guichard and Mongon (2000). The gustiness is added to the wind velocity which enters the flux computation. Over ocean, the surface roughness z_0 is affected since it depends on the surface wind stress.

3.8. Gravity Waves

In LMDZ, nonorographic gravity waves parameterizations were introduced more than 10 years ago when the model was extended upward to the middle atmosphere (Lott et al., 2005). At that time, the parameterization used did not identify the gravity waves source and was also based on a fully spectral approach due to Hines (1997). Since then, we have replaced this parameterization by two distinct parameterizations that account for gravity waves from convection (Lott & Guez, 2013) and fronts (de la Cámara & Lott, 2015). These parameterizations use a multiwave stochastic approach that allows to launch large ensembles of gravity waves in a very intermittent manner. This intermittency proved out to be extremely beneficial for the model climate in the middle atmosphere and in the simulation presented here the nonorographic gravity waves setup is close to that documented in de la Cámara et al. (2016).

4. Configurations and Tuning

A reference configuration of a climate model such as these derived by the various groups for CMIP exercises is not only a question of model content but also of the choice of a grid configuration and tuning of model free parameters.

4.1. Grid Configurations

Concerning the grid configuration, the last three CMIP exercises have been marked, each time, by a significant increase in the resolution of the vertical grid for the IPSL model. From the CMIP3 to CMIP5 exercise, the vertical grid was changed from 19 to 39 layers with, as a major target, the extension to the stratosphere (Hourdin et al., 2013). The 79-layer vertical discretization (L79) used for the CMIP6 configuration was designed to improve the representation of the stratospheric circulation, with an upper layer located at about 80 km above surface. The resolution was also improved in the first kilometers to better represent the boundary layer transport and associated clouds. In the L79 configuration, the first layer is centered at 10 m above surface. In the first 3 km above the surface, the layer thickness δz varies almost linearly with altitude with $\delta z \simeq 0.11 z$ so that 25 model layers are dedicated to the first 2 km. The corresponding vertical discretizations are illustrated in Figure 1.

The horizontal grid was also refined through time. The resolution is given here in number of points equally distributed in both longitude and latitude. From a resolution of 96×72, or a resolution of $3.75° \times 2.5°$ for the LMDZ4 grid used for CMIP3, the resolution was increased in latitude for the low-resolution configuration of CMIP5 (96×96, or $3.75° \times 1.9°$). We will denote this configuration $LR^{(5)}$hereafter. With this choice,

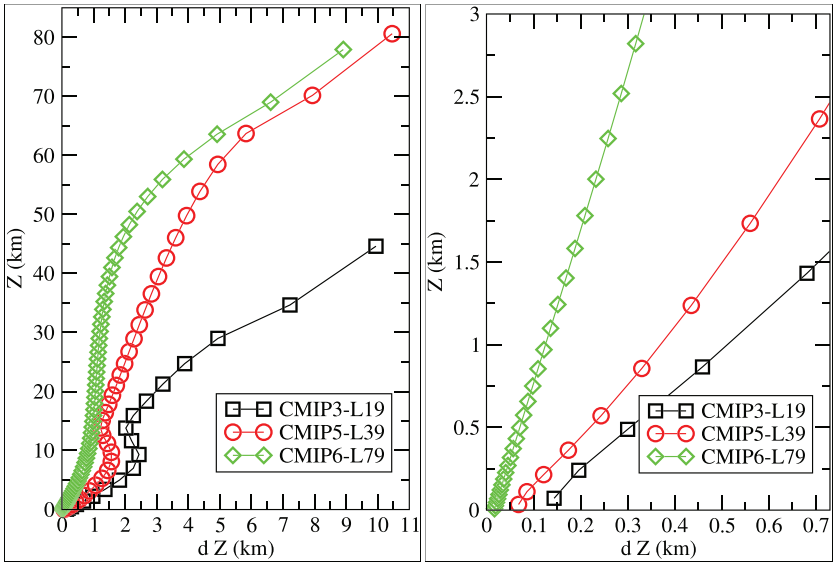

Figure 1. LMDZ vertical grids used for the reference configurations of the successive phases of the CMIP exercise with the IPSL model showing the altitude in *y* axis as a function of the layer thickness in *x*. A focus on the first 3 km is shown in the right panel.

the grid cells are two times more elongated in longitude than in latitude at the equator and isotropic at 60° latitude while the resolution was isotropic at 45° latitude with the LMDZ4 grid. This choice was made because increasing resolution in latitude more than in longitude was shown to push the zonal westerly jets farther toward the poles, in part correcting a classical tendency of global models to locate those jets too close to the equator (Hourdin et al., 2013). For the 5A model, a medium-resolution configuration $MR^{(5)}$ was used as well with 144 × 143 points or 2.5° × 1.25°.

For CMIP6, the $MR^{(5)}$ horizontal grid was considered as the low-resolution grid, called LR or $LR^{(6)}$ hereafter. For the HighResMIP part of CMIP6, a high-resolution configuration was designed with 512 × 361 points, to reach an isotropic resolution of 50 km at 45°. An intermediate grid resolution MR (256 × 257) was also designed but was not used for CMIP6 production.

The characteristics of the CMIP reference configurations of the LMDZ and IPSL-CM model are summarized in Table 1.

Table 1
Characteristics of the Configurations of the LMDZ Model Used as the Atmospheric Component of the IPSL Coupled Model for CMIP Successive Phases

Configuration	Horizontal grid	Vertical grid	Physics content	Name
CMIP3	96 × 71	L19	Convection: from Tiedtke to Emanuel	4
			Subgrid-scale orography	
	$LR^{(5)}$: 96 × 96	L39	Standard Physics (SP): same as LMDZ4	5A
CMIP5	$MR^{(5)}$: 144 × 142	Extension to stratosph.	"New Physics" (NP) = SP +	5B
			thermals and cold pools	
			+ ALE/ALP closure for deep convection	
	VLR: 96 × 96	L39	Standard Physics (SP): same as LMDZ4	5A2
		L79	"New Physics" (NP) +	6A
CMIP6	LR: 144 × 143	$\delta z/z \simeq 0.11$, for $z < 3$ km	New radiation: RRTM + SW 6 bands	
	MR: 256 × 257	$\delta z/z \leq 1$ km, for $z < 50$ km	Stochastic triggering of deep convection	
	HR: 512 × 361		Stratocumulus from thermal plumes	
			Ice thermodynamics	
			Improved coupling with surface	
			Non orographic gravity wave	

4.2. Time Marching

Various time steps and time marching schemes are used for various parts of the model. In order to save computer resources, time steps are often chosen at the limit of numerical stability rather than close to numerical convergence for decreasing time steps as should be the case (Wan et al., 2015).

The time marching of the dynamical part of the model is based on an explicit leapfrog scheme, $X(t+\delta t) = X(t-\delta t)+2\delta t M[X(t)]$ where X is the model state vector, M the numerical model giving the time derivatives of X, and δt the model time step. Every N_{period} step, a Matsuno scheme is applied to reconcile the two solutions corresponding to odd and even time steps that would diverge otherwise. It consists in computing a first approximation of X with a forward scheme $X^*(t+\delta t) = X(t)+\delta t M[X(t)]$, followed by a backward scheme $X(t+\delta t) = X(t)+\delta t M[X^*(t+\delta t)]$. At the beginning of the Matsuno time step, only one of the odd and even solutions are kept. It is the time at which tracer advection, horizontal dissipation, or physical parameterizations can be called. This defines the main model time step $\Delta t = N_{\text{period}}\delta t$. For the dynamical core, the effective number of computations of M is $N_{\text{period}} + 1$ per time step Δt.

The model time step is conditioned by a CFL criterion on the fastest propagating gravity waves. It must be reduced linearly with respect to the smallest horizontal length explicitly represented. For the LR[5] and MR[5] horizontal grids, N_{period} was fixed to 5, with Δt =15 min for LR[5] and Δt = 10 min for MR[5]. For the 6A-LR configuration, it was found to be possible to save some resources by using $(\Delta t, N_{\text{period}})$=(15 min,7) instead of (10 min,5).

With regard to the frequency of calls to the physical parameterizations, the SP physics of LMDZ5A, which was robust but not very reactive, ran with time steps of 30 min. On the contrary, the LMDZ5B version was very unstable. The main model time step Δt = 15 min of the 5B-LR[5] version had to be split in two physical time steps of 7.5 min each for the 5B version.

When developing the new 6A version, the numerical integration of the TKE prognostic equation had to be revisited as explained in Vignon et al. (2018). In summary, the source and sink terms associated with wind shear and buoyancy flux are first added to the TKE with an explicit time scheme. Then the dissipation term in the TKE equation, which takes the form $\partial_t(TKE) = -c\,(TKE)^{3/2}$, is computed with an exact time resolution over one physics time step, considering c, which scales with the inverse of the turbulent mixing length, as a constant (the diffusion equation, once eddy diffusivity is known, is integrated in time with an implicit time scheme in all the versions.): $TKE_{t+\delta t}^{-1/2} - TKE_t^{-1/2} = -c\ \delta t/2$.

The computation of downward transport in the environment of the thermal plumes was modified as well using an implicit time scheme and upwind scheme. With those two changes, it was possible to keep a 15 min time step for the physics in LMDZ6A.

Illustrations of the effect of those modifications are given in Figure 2 which shows the comparison of single-column-model integration of LMDZ with LES for three classical test cases and for the successive model physics with various time steps. Improvements come both from the model physics and numerics: The main improvement for the 5B version compared to 5A is the appearance of cumulus clouds. However, even with a 7.5 min time step, results are still noisy. Even if this noise is not fully removed, the modifications of the numerics described above that define the 5B^s ("s" standing for stable) version lead to a significant improvement. The main improvement from 5B^s to 6A concerns the representation of the transition case. While the stratocumulus deck was staying close to the surface during the three days with 5B^s, the new scheme represents reasonably well the growth of the boundary layer and the appearance of two distinct cloud maxima with a marked diurnal cycle. The change is not due to the increased vertical resolution but to the activation of the mass flux scheme, which was deactivated in this case for the 5B^s version. The comparison of the 7.5 and 15 min time steps for the 6A case still shows some sensitivity to the numerics. Tests with other vertical resolutions and more complete evaluation of the 6A physics on this transition case can be found in Hourdin et al. (2019).

Radiation was called every 1 hr in the 5A and 5B versions and only every 1.5 hr in LMDZ6A. This choice was made because 1.5 hr is also the time step for coupling with the ocean in IPSL-CM6A (the coupling was done only once a day in the CMIP5 versions). In the 6A version the deep convection scheme is called only every two physics time steps, that is, every 30 min to save additional computer time. It was checked in both SCM and GCM mode that the use of a longer time step for radiation and convection does not alter the behavior of the model significantly.

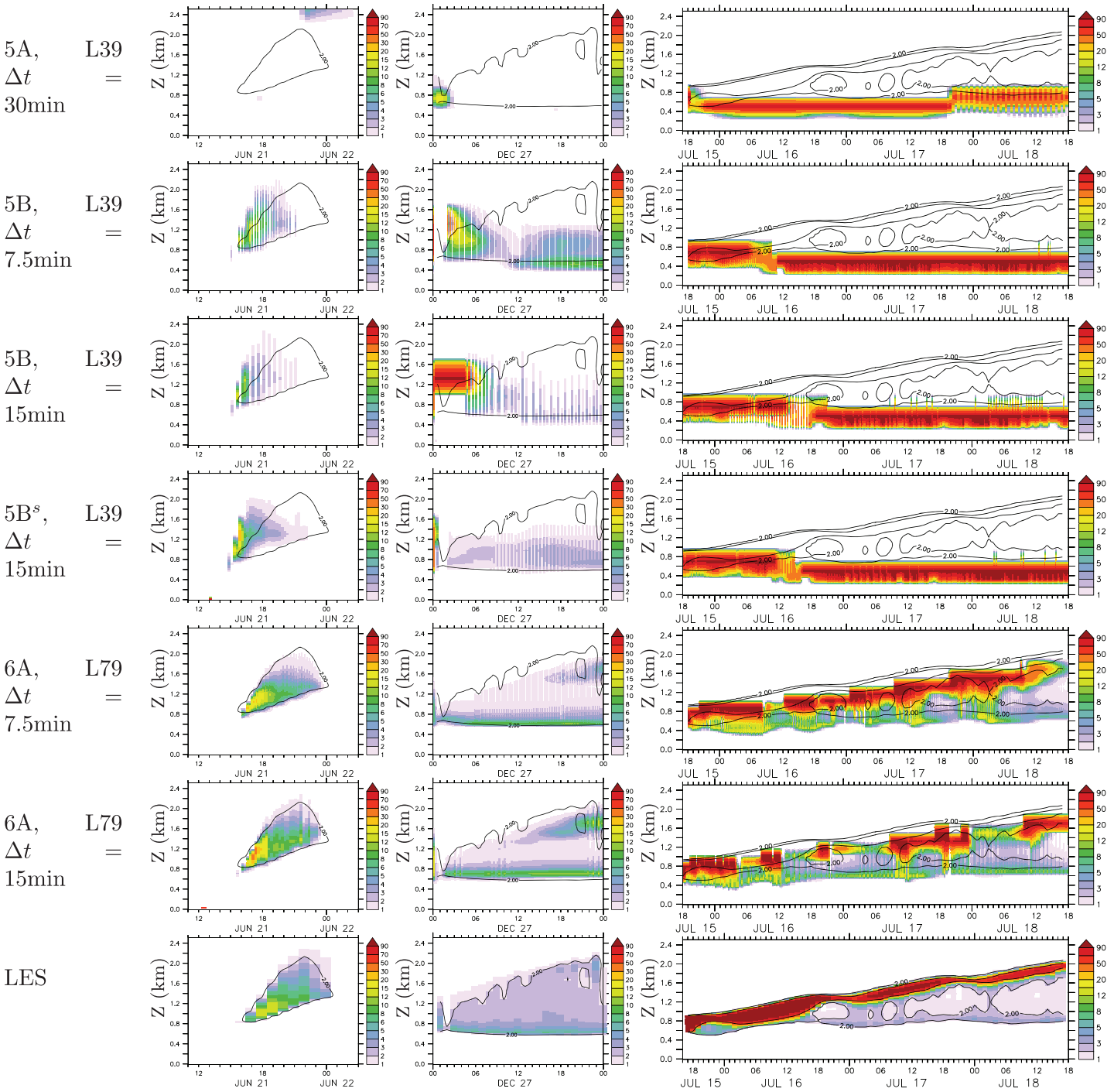

Figure 2. Time evolution of the cloud fraction vertical profile obtained with the various model configurations for three LES test cases and various time steps. The setup is given at the beginning of each row of the figure. The last row shows LES results. The first two columns correspond to a continental and oceanic cumulus case. The continental ARM case is derived from observations collected on 21 June 1997 at the Atmospheric Radiation Measurement site in Oklahoma, USA (Brown et al., 2002). The RICO experiment (RICO for Rain In Cumulus over the Ocean) focuses on precipitation processes at play in trade wind shallow cumulus. For the ARM and RICO cases, LES are performed with the Meso-NH nonhydrostatic model (Lafore et al., 1998; Lac et al., 2018). The third column shows the REF composite stratocumulus to cumulus transition case discussed by Sandu and Stevens (2011) with a reference LES performed with the UCLA model. The figures display all the time steps explaining the finer peaks in the experiments with time step of 7.5 min. The LES results were available with a 1-hr time frequency.

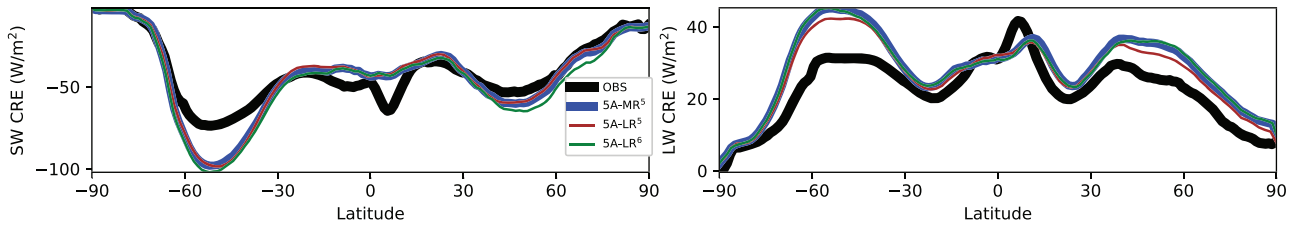

Figure 3. Zonal and annual average of the shortwave (SW, left) and longwave (LW, right) cloud radiative effect (CRE, W m^{-2}) for the 5A physics, showing results from the "amip" 5A-LR[5] (brown) and 5A-MR[5] (blue) simulations available on the CMIP5 archive and a recent "clim" 5A-LR[6] simulation (green) forced by climatological SSTs. The black curve corresponds to the second edition of the CERES-EBAF L3b product used as a reference for radiative fluxes for model evaluation and tuning (Loeb et al., 2009).

With these choices and after some optimization work, the LMDZ6A-LR model can simulate about 20 years per day of elapsed time. Technically, simulations are run on supercomputers made available by the French HPC centers, either a Bull Sequana X1000 with bisocket nodes composed of Intel Xeon 8168 (SKL) at 2,7 GHz (24 cores by socket, 48 cores by node) and 192 Gb of RAM or a IBM x3750, quad-socket nodes composed of quad-cores Intel Sandy Bridge (E5-4650) at 2.7Ghz (32 cores by nodes) and 144 Gb of RAM. Computing performance is achieved by domain decomposition parallelism on the horizontal layer using message passing interface (MPI) library, and using shared memory parallelism (openMP) either across vertical level loops (dynamical part) or across horizontal loops (physical part). For the LMDZ6A-LR resolution, the best compromise between resources and performances is found when using 71 MPI processes with 8 openMP threads running onto 568 cores. The performance of the model falls to about 16 simulated years per day when the full CMIP6 workflow is activated (accounting for output and postprocessing).

4.3. Backward Compatibility

During the development phase of the configuration of the model for CMIP6, a priority was given to backward compatibility. It is indeed possible to rerun the configurations used for CMIP5 and even CMIP3 with the last versions of the source files. Even some bugs that were shown to significantly affect the model behavior were maintained in the code under "flags" for that purpose. Running an old configuration with the last version of the source code is powerful when trying to disentangle how some model changes impact the simulated climate. Of course, this backward compatibility adds complexity in the code but our recent experience has shown that it is more efficient in the end.

Table 2
Characteristics of the Simulations Used in This Paper

Name	Δt		Δt_{phys}	τ_h	τ_{rot}	τ_{div}			
Unit	(min)	N_{period}	(min)	(hr)	(hr)	(hr)	clim	amip	HighRes
5A-LR[5]	15	5	30	1.5	1.5	1.5		X	
5A-MR[5]	10	5	30	1.5	1.5	1		X	
5A-LR[6]	10	5	30	1.5	1.5	1.5	X		
5B-LR[5]	15	5	7.5	1.5	1.5	1.5		X	
5B[s]-LR[6]	15	5	15	1.5	1.5	1		X	
6A-LR	15	7	15	3	6	1	X	X	X
6A-HR	3.75	7	15	1/4	1/4	1/6	X		X

Note. The main model time step Δt is divided into N_{period} steps for the dynamics. Δt_{phys} is the time step of the physics. The time constants for horizontal dissipation are also shown. The dissipation is computed with a Laplacian operator iterated twice for potential temperature and rotational component of the horizontal wind with dissipation time constants τ_h and τ_{rot} for the smallest horizontal scale explicitly represented in the model δx_{min}. The wind divergence is dissipated with a single Laplacian operator with time constant τ_{div}. The simulations used are forced either by a mean seasonal cycle of SSTs for the period 1990–2000 ("clim"), or with the SSTs of the standard "amip" protocol with interannual variability, or with the protocol of the HighResMIP exercise, with SSTs varying daily (denoted "HighRes" in the paper).

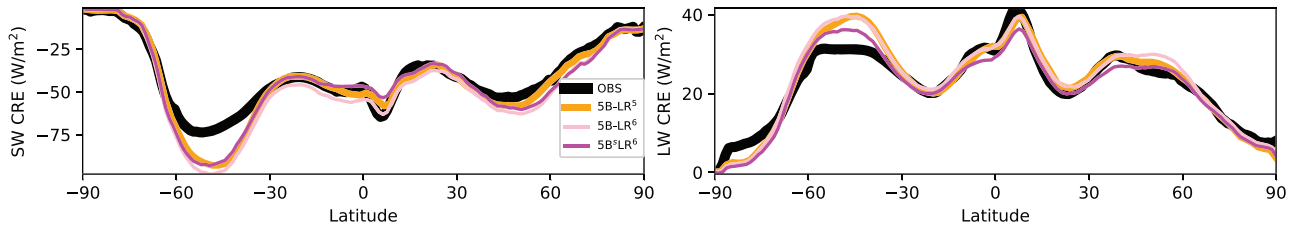

Figure 4. Zonal and annual average of the shortwave (SW, left) and longwave (LW, right) cloud radiative effect (CRE, W m^{-2}) for the "amip" 5B-LR^5 simulation available on the CMIP5 archive (orange) and for recent simulations forced by climatological SSTs with the 5B physics ("clim" 5B-LR^6, pink) and a stabilized version of it ($5B^s$-LR^6, magenta). The black curve corresponds to CERES-EBAF observations.

It is thus possible to rerun the 5A and 5B versions of the model with the source files of the 6A version just by changing a "namelist" file named "physiq.def" that controls the switch between parameterizations as well as the values of the physics-free parameters.

To illustrate this point, we show in Figure 3 the zonal and time average of the shortwave (SW, left) and longwave (LW, right) cloud radiative effect (CRE). For the 5A-LR^5 and MR^5 configurations, we take results directly from "amip" simulations on the CMIP5 archive. We compare them with a 5A-LR^6 simulation run on climatological SSTs with the 5A physics but the most recent source files (details on the simulation setup are given in Table 2). Despite the change of surface scheme, of source codes, and of boundary conditions, the blue and green curves (run with same grid LR^6 or LR^5) are almost superimposed. The main difference is the increased SW CRE in northern midlatitude. The impact of the use of annually varying SSTs versus climatological SSTs was independently tested and found to have negligible impact on this diagnostic (not shown). For the LW CRE, the change is systematically less than the change of resolution from LR^5 to MR^5 grid in CMIP5.

For the 5B physics, we show in Figure 4 the comparison between results obtained with the LR CMIP5 grid and the old source code version (taking the results from the CMIP5 archive) and with the LR CMIP6 grid and the new source code, as well as a simulation on the CMIP6 grid run with the stabilized version of the boundary layer scheme $5B^s$. The difference between the three simulations is generally small compared to the difference between the results of the 5A and 5B versions. In particular, the latitudinal variation of both the SW and LW CRE in the tropics is much better represented with the 5B version. The better representation of the LW CRE in the midlatitudes, which was strongly overestimated for the 5A version, is robustly reproduced with the recent source codes, as well as with the stabilized model. The remaining differences between the 5B-LR^5 and 5B-LR^6 versions may have several origins: modification in the surface scheme, change in horizontal resolution, or some bug corrections not flagged in the model.

Nevertheless, these diagnostics and others not shown demonstrate that we are able to reproduce simulations similar to the CMIP5 5A and 5B configurations.

4.4. Tuning of Atmospheric Radiation

As was already the case for the derivation of the CMIP5 versions of the model, particular care was given to the tuning of model free parameters.

Like many climate modeling groups (see the survey presented in the supplementary material of Hourdin et al., 2017), we focus our tuning efforts on the most uncertain parameters which have the strongest effect on radiative balance at the top of the atmosphere (i.e., the cloud parameters). A list of the main parameters used for tuning of the LMDZ6A model is given in Table 3. The global energy balance is targeted because it directly controls the global mean temperature in the coupled atmosphere-ocean model. The individual SW and LW fluxes and their decomposition into clear-sky radiation and CRE are also considered. In addition to global values, latitudinal distributions which control the global circulation are also considered as well as the link between radiation and dynamical regimes in the tropics.

In Figure 5, we compare with observations (black) the latitudinal variation of the LW, SW, and total (TOT) CRE at top of atmosphere, the outgoing SW (OSR) and LW (OLR) radiation and the mean rainfall for the 5A (blue), 5B (orange) and 6A (red) versions of the physics, all run on the LR^5 grid. The results of the HighResMIP 6A-HR simulation (green) is shown, as well as the results of the CMIP6 multimodel "amip"

Table 3
List of Main Parameters Used During the Tuning of Global Atmospheric Simulations Forced by SST

Name	Range	6A	Unit	Comment
$wk_{\text{dens,oce}}$	$[10^{-11}, 10^{-8}]$	$1.e^{-9}$	m^{-2}	(fixed) wake density over oceans
$\gamma_{\text{Alp,th}}$	[0.2, 0.8]	0.5		$Alp = \gamma_{\text{Alp,th}} \times ALP_{\text{thermals}} + \gamma_{\text{Alp,wk}} \times ALP_{\text{wake}}$
$\gamma_{\text{Alp,wk}}$	[0.01, 0.5]	0.25		
$\text{cld}_{\text{l,conv}}$	[0.1, 1]	0.65	g/kg	threshold for conversion of cloud liquid water to rainfall
$\gamma_{\text{fall,v}}$	[0.3, 2.]	0.8		scaling factor on the fall velocity of ice crystals
p_{0_r}	[300, 600]	450	hPa	width of the subgrid-scale distribution of total water q_t is $\sigma_{q_t} = r \times q_t$
Δp_r	[50, 300]	100	hPa	where r varies between $r_{\min}$ (= 0.002) and $r_{\max}$ with decreasing
$r_{\max}$	[0.05, 0.6]	0.4		pressure P as $r = r_{\min} + (r_{\max} - r_{\min})\{\tanh[(p_{0_r} - P)/\Delta p_r] + 1\}/2$
b_0	[1, 2]	1.3		droplet number concentration CDNC $= 10^{b_0 + b_1 \log(q_{\text{aer}})}$, $b_1 = 0.2$
				q_{aer} being the concentration of soluble aerosols in $\mu g/m^3$
σ_{cvpr}	[0.001, 0.02]	0.003		Grid cell fraction covered by unsaturated precipitating downdrafts
$w_{B,\text{srf}}$	[0.05, 2.]	0.5	m/s	Deep convection vertical velocity at cloud base (m/s)
$w_{B,\max}$	[1.5, 6]	2.8	m/s	$w_B = w_{B,\text{srf}} + w_{B,\max}/[1. + 500/(P_s - P_{\text{LFC}})]$, where P_s and P_{LFC}
				are the surface and "Level of Free Convection" pressure in hPa.
$EP_{\max}$	[0.9, 0.9999]	0.999		Rainfall efficiency for deep convection is
$q_{\text{l,crit}}$	[0.1, 2]	0.3	g/kg	$EP = \min\{\max[1. - q_{\text{l,crit}} * (1.0 - T/T_{\text{l,crit}})/q_{\text{liq}}, 0], EP_{\max}\}$
$T_{\text{l,crit}}$	[-65,-35]	−55	°C	where q_{liq} is the incloud liquid water (in g/kg).
λ_d	[0.05, 0.15]	0.07		$z^* = z + \lambda_d z$ for plume detrainment, see Section 3.2

Note. For each parameter, the typical minimum and maximum values authorized during the tuning process are given, as well as the value finally kept for the 6A configuration. This authorized range arises from the expertise of the parameterization developers.

simulations available on the IPSL data center when this paper was submitted (gray curves). The improvement observed between 5A and 5B regarding the latitudinal variation of the CRE in the tropics is amplified with the 6A version. Part of the improvement probably comes from the modification of the physics content and better representation of low clouds as documented by Hourdin et al. (2019), but part of it also comes from a better tuning. The tuning is however so directly linked to cloud representation that it is not possible to quantify the relative importance of improvement and tuning in this case.

In Figure 6, the bias (+ signs), the root-mean-square error computed from the annual and zonal means (RMSz, circles) and from the mean seasonal cycle of the longitude-latitude varying fields (RMSg, squares) are shown for the same variables as in Figure 5. The same metrics are computed as well for all the CMIP6 and CMIP5 simulations available. Comparing the CMIP models is a way to (1) assess model improvements objectively; (2) give an idea of the significance of an improvement by comparing it with the CMIP models; and (3) identify some systematic biases shared among models and improvement (or not), through time, of the model ensemble.

Concerning the top of the atmosphere global fluxes (OSR, OLR, SW, and LW CRE), there is a significant improvement from version 5A (SP) to 5B and from 5B to 6A. This is a consequence of the improvements in cloud representation (Hourdin et al., 2019) and better tuning. There is also a general improvement between the CMIP5 and CMIP6 ensembles. Note that with the exact same tuning, the radiative metrics are quite similar for the LR and HR versions of IPSL-CM6A despite a large gap in horizontal resolution.

4.5. Tuning of Precipitation

While a strong effort was made for 5A and 5B to find parameters that reduce the global mean rainfall, this target was abandoned for the tuning of the 6A version with a clear consequence on the ranking of this version compared to CMIP5 and CMIP6 models shown in the last panel of Figure 6. Note that the model ranking would be very similar if considering the global mean rainfall bias (positive for all models) rather than the RMSz, suggesting that a large part of the RMS error is due to the general overestimation of rainfall by the models. This puzzling systematic overestimation still lacks explanation and is the main reason for not putting too much emphasis on it for the CMIP6 tuning. Since the GPCP precipitation estimate

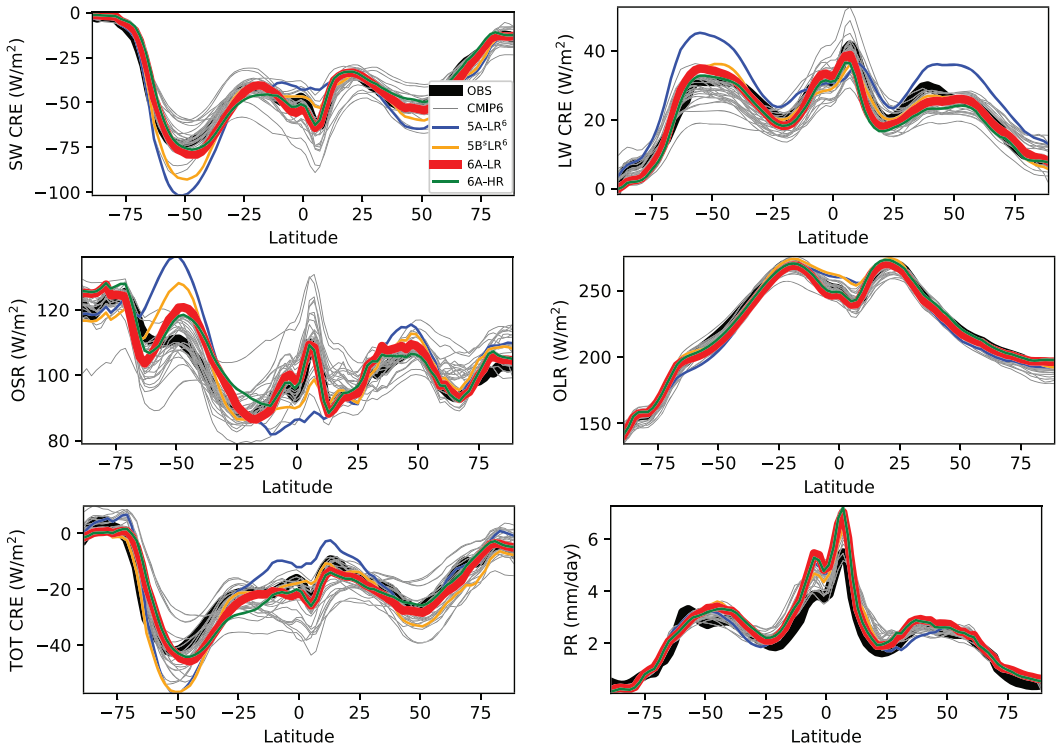

Figure 5. Zonal and annual averages of the longwave (LW CRE), shortwave (SW CRE), and total (TOT CRE) cloud radiative effect, of the top of the atmosphere outgoing shortwave (OSR) and longwave (OLR) radiation (all fluxes in W m^{-2}), and surface precipitation rate (PR, mm/day) for the "clim" simulations 5A-LR^6 (blue), 5B-LR^6 (orange, see Table 2 for details), and CMIP6 "amip" simulations: IPSL-CM6A (red) and other models participating to CMIP6 (gray curves). The black curve corresponds to CERES-EBAF observations for radiative fluxes and to the Global Precipitation Climatology Dataset for the last panel (GPCP, Huffman et al., 2001).

has been shown to be inconsistent with observed radiative fluxes (Kato et al., 2011), the overestimation of total precipitation in the model may be partly due to an underestimation of observed precipitation due to an underestimation of light rain that may reach 10% (Stephens et al., 2012) in particular over the Indian Ocean, the SPCZ and ITCZ (Berg et al., 2010). However, this is probably not enough to explain the 15% overestimation of the global mean rainfall in LMDZ6A compared to GPCP.

Although global-average precipitation bias was not a tuning target, several regional characteristics were. The rainfall over Sahel, which was strongly underestimated in previous version, was seen as a target for improvement. The number of days without rainfall over the ocean was also considered to try to correct the general tendency of the model to produce at least some rainfall every day everywhere over tropical oceans. Increasing the cold pool density over the ocean (constant so far) was key to achieving this goal. This change degraded the representation of rainfall over the continents, however. To fix this, the cold pool density was finally fixed to 10^{-9} (one cold pool per (32 km)^2) over the oceans and 8 10^{-12} (one cold pool per (350 km)^2) over the continents, which is consistent with an observed tendency of the cold pools to be much denser and smaller over the oceans. Note that a prognostic model of cold pool density is currently being tested in LMDZ.

Despite attempts to improve the Madden Julian Oscillation or ENSO (in coupled model) variability, this target was abandoned during the tuning phase. The tuning of rainfall monsoon and variability was done mainly with the parameters that control the ALE/ALP closure of the deep convection scheme. One of them, $w_{B,\max}$, is a maximum value for the vertical velocity at cloud base w_B. As explained by Rio et al. (2013), the larger this velocity, the more difficult it is to provide enough energy and power from the subcloud processes to activate deep convection. Increasing w_B increases the rainfall intermittency but tends to reduce rainfall over semi-arid regions like Sahel. This w_B is already imposed as a vertical profile that increases from $w_{B,\mathrm{srf}}$ at the surface to $w_{B,\max}$ in order to account for the fact that convection over tropical ocean with very low cloud base has smaller vertical velocity at cloud base than convection over semiarid region like Sahel in which the cloud base is located several kilometers above the surface. Note that using too large values of $w_{B,\max}$ close to

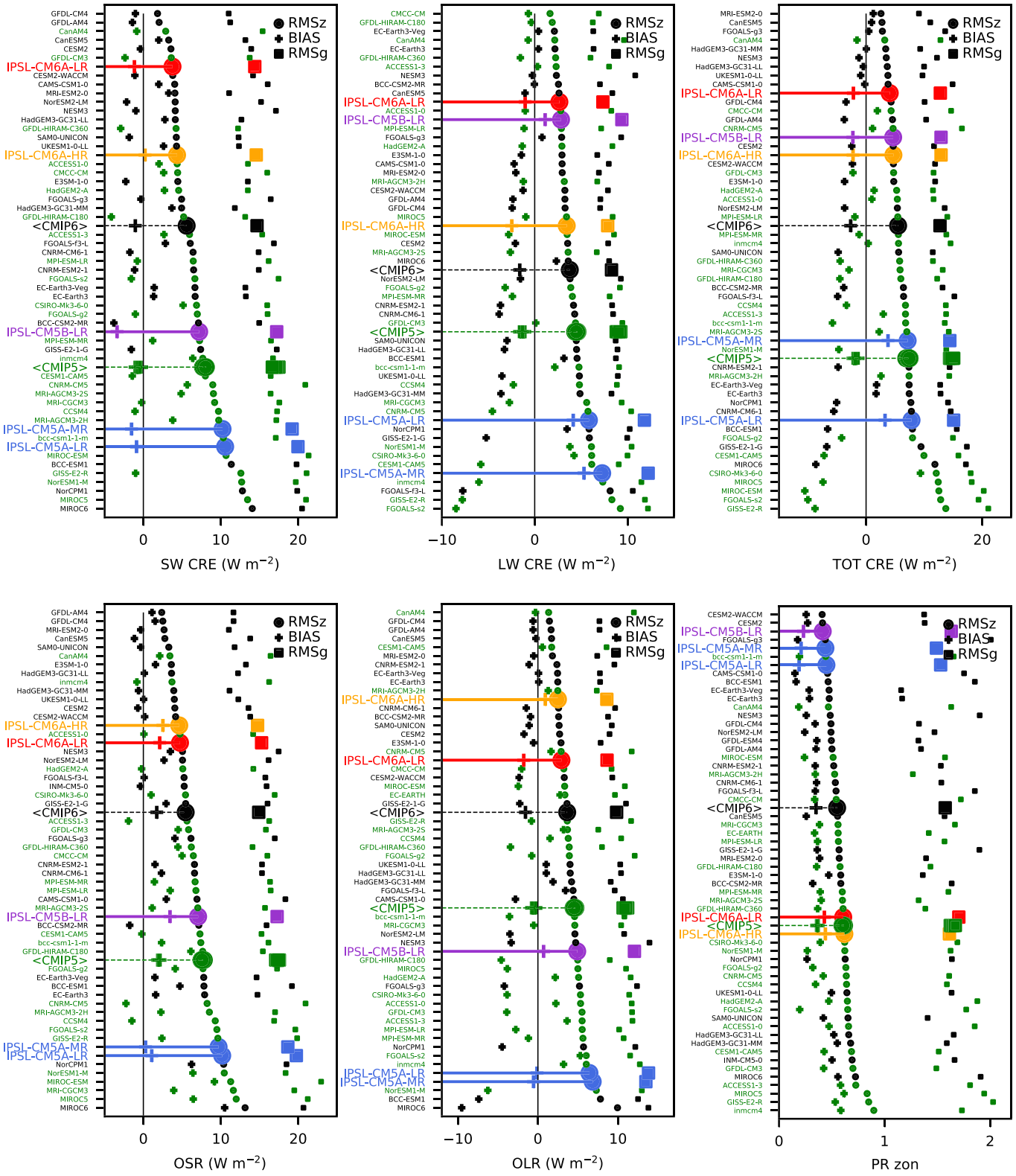

Figure 6. Root-mean-square error computed on the annual zonal mean (RMSz, circles), global mean bias (+ signs) and global root-mean-square error computed on the mean seasonal cycle of the longitude-latitude varying fields (RMSg, squares) for longwave (LW CRE), shortwave (SW CRE), and total (TOT CRE) cloud radiative effect, outgoing shortwave (OSR), and longwave (OLR) radiation (W m^{-2}) and for the precipitation rate (PR, mm/day) for the CMIP5 and CMIP6 models. Models are ranked according to RMSz. The metrics are computed with respect to the EBAF and GPCP climatologies. The names and ranking of CMIP models are given in Table A1 for CMIP5 and Table A1 for CMIP6.

the surface over the oceans helps to increase the rainfall day-to-day variability but the additional rainfall is mainly explicitly resolved, which is not reasonable for grid cells more than 100 km in length.

The tuning of rainfall was not pushed as far as intended partly due to a lack of time, partly due to doubts on the relevant metrics and observations, and also due to the fact that tuning of convection is strongly coupled to the tuning of radiation. Some parameters of the convective scheme strongly impact radiation, for example, the maximum efficiency of precipitation EP_{max}, a parameter close to 1 which directly controls the fraction 1-EP_{max} of cloud water that detrains in the upper atmospheric layers. In turn, radiation is key for the control of convection. Being able to jointly tune radiation and convection is probably something which cannot be handled with small series of sensitivity experiments and manual tuning, but will require the help of machine learning techniques like uncertainty quantification approaches (Williamson et al., 2013). Further parameterization developments are likely still needed in order to more physically represent high-level clouds associated with deep convection and their life cycle.

A summary of the main parameters used for tuning with available values is given in Table 3.

4.6. Other Targets for Tuning

A number of iterations were done between the tuning of the atmospheric model and the changes in the land surface model, which evolved quite heavily during the development of the CMIP6 version of the model, making the tuning of the coupled land-atmosphere model challenging. The main effort was put on the representation of mean seasonal cycle of temperature. The bare soil albedo map and the individual albedo of the 14 plant functional types of the Orchidee model were adjusted directly by tuning to MODIS observations.

A specific tuning focus was put on polar regions. This was stimulated by participation in the fourth intercomparison exercise of the Gewex Atmospheric Boundary Layer Study (GABLS4, Bazile et al., 2014). Using 1-D simulations during a typical summertime diurnal cycle at Dome C, East Antarctic Plateau, the "land-ice" (terrestrial icy surface type) surface scheme and the turbulence parametrization of LMDZ were tuned according to several criteria among which the amplitude of the temperature diurnal cycle, the height, and strength of the nocturnal jet and the values of the surface turbulent fluxes (Vignon et al., 2017). Further sensitivity tests were also carried out using 3-D simulations with a stretched-grid over Dome C. The latter made it possible to assess the representation of the vertical structure of the very stable wintertime boundary layer as well as the sharp dynamical transitions of the temperature inversion between the weakly stable and the very stable state of the boundary layer (Vignon et al., 2018).

The first main change in terms of surface parameters affects the thermal inertia of the snow that covers the ice sheets surface. Its value was changed from a typical value for pure ice to a more realistic value for dense snow. Likewise, the albedo of land-ice surfaces was corrected from an unrealistically low value that was set in LMDZ4 to compensate for a lack of downward longwave radiative flux at the surface of the ice sheets. Momentum and heat roughness length values over land-ice set at 1 mm in LMDZ5 were not changed since they were shown to be reasonably well representative of measurements performed over the Antarctic and Greenland ice sheets.

The calibration of LMDZ over Antarctica mostly guided the changes of the turbulence and surface layer schemes for very stable conditions (cf. Section 3.1). Overall, the abovementioned changes have led to a more realistic summertime diurnal cycle of the polar boundary layer, colder winter and closer-to-observations surface temperature over Antarctica, sharper and more realistic transitions between the weakly stable and the very stable state of stratified boundary layers as well as a stronger climatological surface-based temperature inversion over the Antarctic continent.

Finally, several aspects of the tuning process targeted identified problems of the coupled atmosphere-ocean models. Tuning the coupled model involved many scientists and was a 2-year process during which 15 successive versions of the coupled model were tested with centennial simulations. The atmospheric model was retuned for each version. The coupled model tended to systematically underestimate the sea ice cover and volume over the Arctic ocean. The albedo and conductivity of the sea ice were thus set to their largest allowed values, the most favorable to sea ice formation. Surface fluxes in this region were thus investigated but the lack of metrics and understanding of key processes resulted in a lack of robust progress. Also, parameters of the subgrid-scale orography were modified in order to better represent the stationary nonzonal circulation in the northern midlatitude, the meridional component of which impacts the heat transport over the Arctic ocean. The coupled model also tended to underestimate deep water formation in the North Atlantic and

associated overturning circulation. This point was a target and may have influenced model configurations selection.

A much more direct tuning aimed at reducing classical SST biases. Following Hourdin et al. (2015), specific metrics were applied to the surface fluxes in the stand-alone atmospheric simulations forced by observed SSTs in order to correct major SST biases in coupled simulations: the Eastern Tropical Ocean (ETO) warm bias, present in all CMIP5 models but one, and to a lesser extent the Circum Antarctic warm bias. The SST bias over the ETO in coupled simulations was shown to be strongly correlated in the CMIP5 multimodel ensemble with the biases in surface turbulent and radiative heat fluxes in the stand-alone atmospheric simulations. In simple words, models with a strong SST bias in coupled simulations are those with strong heating of the surface by the atmosphere in forced mode (it does not hold if considering the flux in coupled mode since the flux and in particular the evaporative cooling strongly responds to the SST bias). In practice, the warm bias can come from an underestimated shadowing effect of clouds, from an overestimated longwave radiation at the surface if, for instance, clouds are too close to the surface, or from a reduced evaporative cooling induced for instance by an overestimated near-surface relative humidity. The SSTs of the coupled model were thus tuned indirectly by tuning boundary layer clouds and convection in stand-alone atmospheric mode. What was targeted is not the absolute value of the associated flux biases but rather the anomaly compared to the rest of the tropics. During the tuning phase of the model, we systematically used the ETO anomaly (ETOA) index of Hourdin et al. (2015) targeting fluxes ETOA as small as possible in order to reduce the SST bias. This strategy was successful and the final ETOA bias was significantly reduced as illustrated in the left panel of Figure 7. Note that the correlation between surface fluxes and SST ETOA in the full CMIP5+CMIP6 ensemble shown in this figure is of 0.85. A similar metric was used for the Circum Antarctic warm bias, inspired by a work by Jones et al (poster at the 2015 Dubrovnik CMIP5 conference). The associated bias was also reduced in IPSL-CM6A-LR when compared to previous versions. The correlation between SST negative anomalies and negative flux anomalies in the stand-alone atmospheric simulations is however only 0.60 in this case (right panel in Figure 7).

Summaries of the free parameters and targets kept for the tuning of the 3-D atmospheric configuration are given in Tables 3 and 4, respectively. These tables relate to the 2-year tuning phase with the global LMDZ6A-LR configuration forced by SST and do not consider the tuning which was done previously or in parallel at process scale like the QBO frequency, the behavior of the turbulent scheme in very stable conditions, or the fraction of supercooled liquid cloud water. In particular, the successive versions and tuning were systematically tested in single-column mode and compared with LES on a series of classical test cases of shallow and deep convection.

Note that the model equilibrium climate sensitivity (ECS) was not tuned. Preliminary transient experiments suggested that it was probably relatively large, but no attempt was made to analyze it nor to find pathways to modify it. The ECS is thus an emerging property of the 6A version as it was for the 5A and 5B versions. This issue will be analyzed in a joint paper on the coupled model (Boucher et al., 2020). Comparing the 5A and 6A configurations, the effective ECS diagnosed from CO_2 abrupt change experiments with the coupled model has increased from 4.1 to 4.8 K, due to an increase in the water vapor and lapse rate feedback combined with a significant decrease in the cloud feedback.

5. Elements of Climatology

Some important elements of the climatology, deficiencies, and skills of the new 6A version of LMDZ compared to previous versions are presented in this section. We only briefly summarize the elements given in companion papers of this Special Collection concerning clouds (Madeleine et al., manuscript 2020MS002046), coupling with continental surfaces (Cheruy et al., manuscript 2019MS002005) and the full coupled model (Boucher et al., 2020). A large emphasis is put on space-time distributions of tropical rainfall which are not described elsewhere. All the diagnostics presented in this section were obtained with the standard "amip" and "HighResMIP" IPSL simulations available on the CMIP5 and CMIP6 databases, except for Figure 14 which is based on short simulations run on climatoloical SSTs.

5.1. Upper Atmosphere

With an upper level at around 80 km and a vertical resolution of about 1 km up to 40 km altitude, LMDZ6A is a "high-top" model.

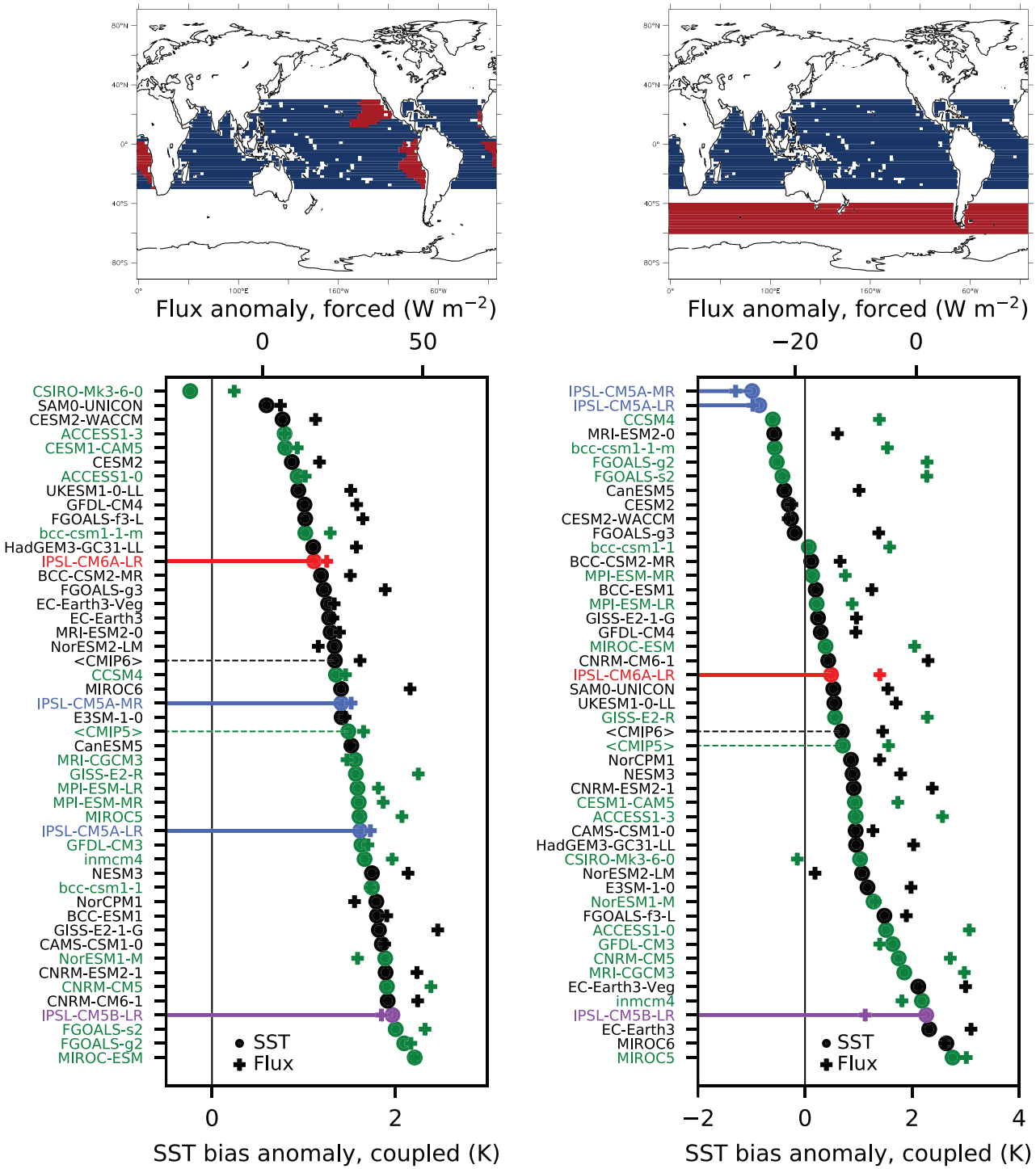

Figure 7. Anomalies in the SST bias in coupled simulations (circles, bottom *x* axis, using "amip" SSTs as an observation) and in surface fluxes in amip simuations (+, top *x* axis) for the East Tropical Ocean (left) and the circum Antarctic ocean (right). The anomalies are computed as the difference between the average over the red and blue areas displayed on the maps of the top panels (the blue area including the red ones for the left one). The ranking of the models is from the most positive (bottom) to most negative value (top) of the anomaly.

Table 4
List of Main Targets of the Tuning of the Global Atmospheric Simulations

Tuning target	Requirement	Comment
	Clouds and radiation	
Global, total TOA	<0.2 W/m^2	Targeting global SST of the coupled model
Global OSR, OLR, SW CRE, LW CRE	<5 W/m^2	EBAF climatology
Latitudinal variations	<10 W/m^2	Zonal mean profiles of same fluxes
Tropical regimes	<20 W/m^2	Same fluxes separating convective/intermediate/subsiding regimes
Cloud cover	investigated	CRE was privileged
	Temperature, humidity and winds	
2 m temperature	target	iteration with land surface scheme + contrast SST-T2m over ocean
Mean zonal atm. temp.	investigated	not a real target
Mean zonal wind	investigated	more specifically the latitude of the jets
Mean zonal humidity	investigated	
Near surface circulation	investigated	high-latitude stationary waves tuned
	Rainfall	
Global rainfall	NO	
Sahelian rainfall	target	≃30% of mean rainfall
ITCZ over oceans	investigated	
Madden Julian Oscillation	investigated	
Number of days without Rainfall over ocean	target	thresholds 1 mm, expert judgment of maps
Rainfall daily variability	target	expert judgment of maps
	Constraints from coupling	
NH September sea ice	target	selection against underestimation
Atl. thermohaline circ.	target	selection against underestimation
ENSO	investigated	
Circum Antarct. and ETO warm biases	<1 K	based on tuning surface fluxes to an accuracy of < 20 W/m^2 in stand-alone atm. simul.
	Trends	
Observed trends	NO	
ECS	NO	
Aerosols indirect effect	tuned	once from a almost zero to low value

Note. Information on the "Requirement" column gives either an indicative value of the maximum authorized error or a "degree of attention": "target," the target was given a lot of attention but with no clear strategy nor metrics; "investigated," the target was identified in regular diagnostics and may have influenced the selection of model versions; "NO," not considered at all. Many other points were not considered, but we underline points which deserve to be known when using the results. It is important to know in particular that the ECS is an emergent property of this model configuration.

Due to this vertical grid, and to the new parameterizations of subgrid-scale nonorographic gravity waves, LMDZ6A is able to simulate the Quasi-Biennial Oscillation (QBO). Figure 8 shows the evolution of the mean zonal wind at the equator as a function of time and altitude as simulated by 6A-LR (top) and in ERA5 reanalysis (bottom). The model internally produces an oscillation with an averaged period near 24 months, which is however biennial rather that quasi-biennial (18 periods on the 36 years of the figure instead of 17 for ERA5). Note that in earlier versions of LMDZ, the QBO is indeed quasi-biennial and that increasing the periods can easily be achieved by decreasing the amplitude of the convective gravity waves launched. Nevertheless, we decided not to retune the scheme accordingly because the oscillation has much stronger eastward winds than in previous versions and also presents some form of stalling of the eastward winds at

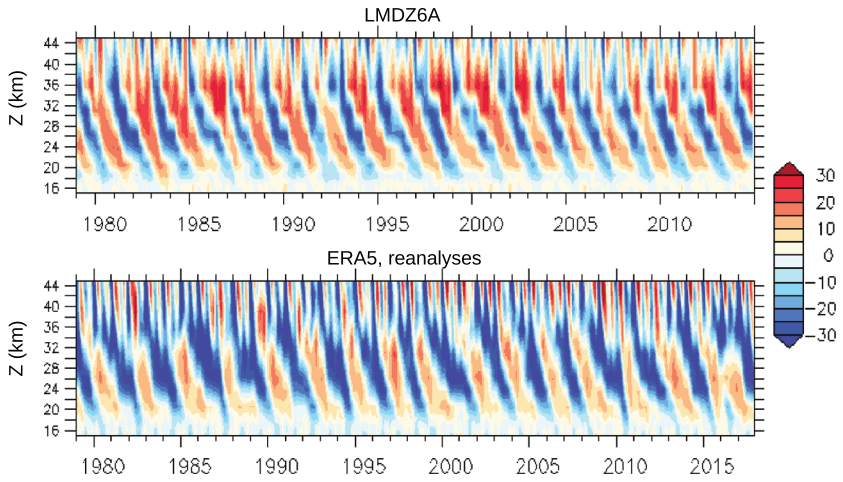

Figure 8. Time-altitude evolution of the zonal mean zonal wind (m/s) at the equator over 30 consecutive years in the LMDZ6A (top) and in the ERA5 reanalyses (bottom).

around 20 km (see, for instance, the year 1986, 1995, or 2000 in Figure 8a), which are more realistic. We thus decided to keep a QBO with an improved structure despite the fact that its period is now shorter than in reality.

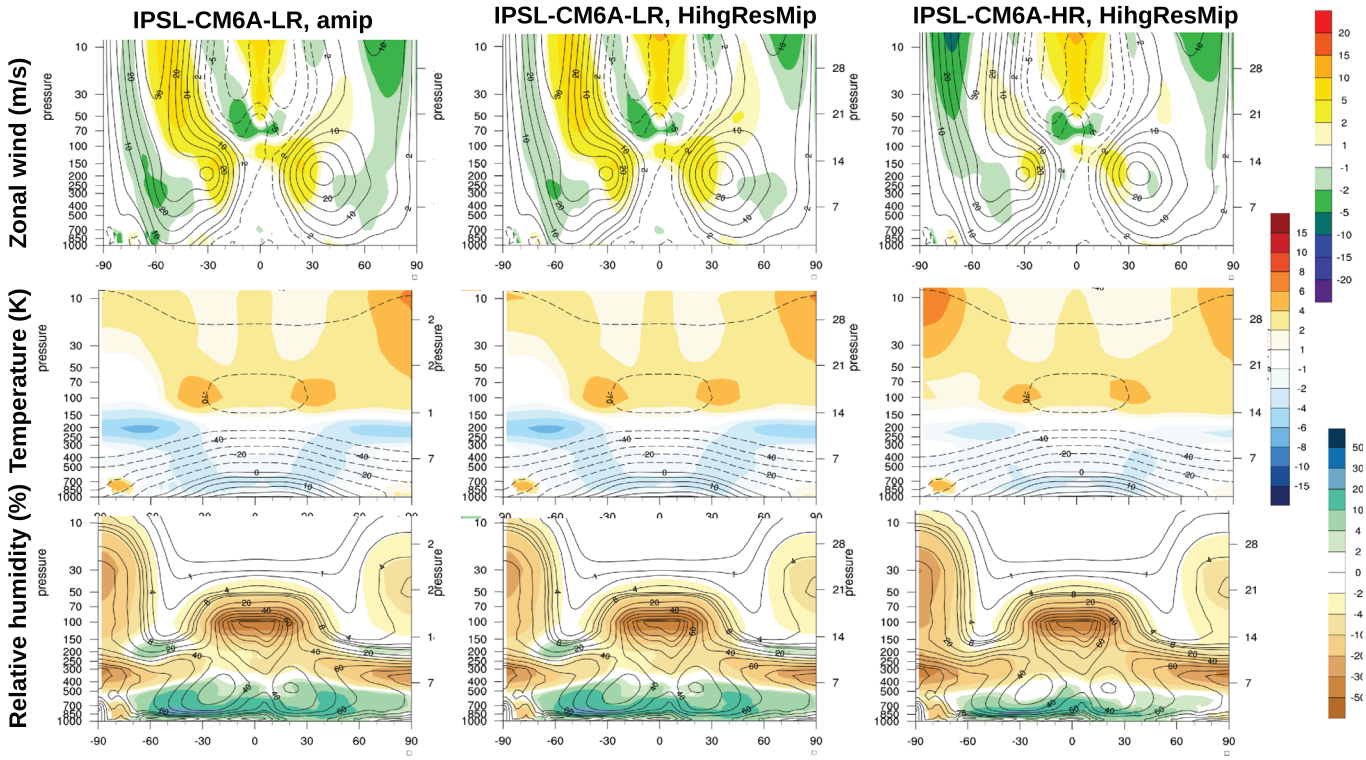

Figure 9. Zonal and annual mean of temperature (K, top), zonal wind (m/s, middle), and relative humidity (%, bottom) in standard IPSL-simulations CM6A-LR (left), HihgResmip-LR (center), and HighResMIP-HR (right). The axis of the ordinates shows the pressure in hPa (left) and an approximate log-pressure altitude in km (right). Contours correspond to the raw fields and the color shades show the difference with ERA Interim analyses (Dee et al., 2011).

5.2. Tropospheric Mean Structure

5.2.1. Winds

The cross section of the annual zonal wind model biases are shown in the top row of Figure 9 for the standard 6A-LR version and for the 6A-HR configuration. The control LR simulation of HighResMIP is also shown since it uses somewhat different forcing in terms of land surface and aerosol specification.

The representation of the annual mean zonal wind has been improved from LMDZ5A (not shown) to LMDZ6A. The jets are however a bit too close to the equator, as seen from the dipolar structure of the bias, with a positive bias on the equator-flank of the jet and a negative bias on its poleward flank. This classical bias of climate models was already shown to be reduced when increasing the horizontal resolution in the 5A version (Hourdin et al., 2013). It is also reduced here when increasing the horizontal resolution from LR to HR. The impact of the differences between the standard Amip and HighResMIP forcing is smaller than the impact of the change in resolution. Note that the jets are better located in the 6A-LR than in the 5A-MR version (not shown here), although they share the same horizontal grid. We are currently still lacking an understanding of this point.

5.2.2. Temperature

The 6A version shows a general cold bias in the troposphere (middle row in Figure 9), particularly marked in the midlatitude and in the lower polar stratosphere, near 200 hPa. This bias was already present in the 5A and 5B versions (not shown).

The latter is well-known in climate models. In previous LMDZ versions, it was shown to be partly due to an overestimated specific humidity leading to an overestimated radiative cooling to space (Hourdin et al., 2006). Consistently with this interpretation, the reduction of this bias (both the cold bias and the associated local wet bias) when increasing the horizontal resolution may be explained by a reduction of the lateral transport of humidity from the tropics by numerical diffusion. The tropospheric midlatitude cold bias is reduced with increasing horizontal resolution together with the improvement of the latitudinal positioning of the zonal jets.

5.2.3. Humidity

The strong wet bias in the lower tropical troposphere (bottom row in Figure 9), when compared to ERAI, was not present in the 5A-LR version. It is caused by a stronger vertical transport of humidity from the surface to the lower troposphere. Globally speaking, the specific humidity is much better mixed vertically in the boundary layer, explaining why the wet bias decreases near the surface. It was shown by Hourdin et al. (2019) that the near-surface relative humidity compares quite well with the climatology of da Silva et al. (1994). It would thus be interesting to compare directly humidity profiles with observations rather than reanalysis to check if the bias in LMDZ may partly be due to an opposite bias in the reanalysis, the vertical humidity profiles over the ocean not being strongly constrained by observations in the latter.

5.2.4. Clouds

The representation of the low-level (Hourdin et al., 2019) and midlevel cloud distributions (Madeleine et al., manuscript 2020MS002046) was signigicantly improved in LMDZ6A. The bi-Gaussian statistical cloud scheme and its new detrainment formulation (see Section 3.2) led to better low-level cloud covers over the tropical oceans (see Hourdin et al., 2019, for further details). The improvement of the deep and shallow convection schemes (see sections 3.3 and 3.2) and the new phase partitioning of cold clouds (see Section 3.4) also result in a better representation of midlevel clouds in LMDZ6A, which were almost inexistent in LMDZ5A. These improvements in the low-level and midlevel cloud distributions are partly responsible for the better CRE shown in Figure 5. However, high-level clouds are underestimated, because a compromise had to be found during the tuning process to restore the radiative balance. As a result, $\gamma_{\mathrm{fall,v}}$, the scaling factor on the fall velocity of ice crystals, is relatively high in LMDZ6A (see Table 3). This suggests that high-level cloud properties must be improved in future versions of the model.

5.3. Surface Couplings

5.3.1. Sea Surface Temperature in the Coupled Model

The better representation of clouds and boundary layer mixing, as well as the tuning strategy presented in Section 4.6, led to a significant reduction of SST biases in the coupled IPSL model. Overall, the metrics

concerning clouds, radiation, and SST have been improved compared to the previous 5A and 5B versions, and are globally satisfactorily reproduced when compared to the CMIP6 ensemble (Boucher et al., 2020).

5.3.2. Coupling With Continental Surfaces

The combined evolution of the atmospheric and the land surface physics led to significant improvements in the representation of the near-surface climate over continents (Cheruy et al., manuscript 2019MS002005).

The individual albedo of the bare soil and of the 14 vegetated plant functional types which is now optimized with respect to MODIS observations is significantly improved especially over desert and semiarid areas where it was significantly underestimated for CMIP5.

The improvement of the radiative balance and in particular the surface downward SW radiation due to better representation of clouds makes it possible to reduce several temperature biases, some of which were shared by many models that participated in the CMIP5 exercise (e.g., summer bias at midlatitude, Stouffer et al., 2017). This confirms the essential role of the radiation and its interactions with clouds for continental climates. The new multilayer hydrology scheme of the Orchidee land surface model (De Rosnay et al., 2002) that substitutes the 1.5-layer scheme used for CMIP5 gives a representation of the surface soil moisture in better agreement with available observations. However, it only moderately impacts the temperature biases when Orchidee is coupled to LMDZ.

In semiarid regions, the improvement of the radiation, the precipitation, and the soil hydrology yielded a significant improvement of the realism of the soil moisture/atmosphere coupling which is in better agreement with the observations. Note that a significant cold bias persists over the Sahara, which may be due to a problem in aerosol forcing, or to the unability to account for a lower-than-one emissivity of the surface in the current radiative code.

5.3.3. Cold Climates

As a result of the snow scheme of intermediate complexity (Boone & Etchevers, 2001) implemented in the land-surface model (Wang et al., 2013), the surface albedo has been improved in most snow-covered region in winter and the strong underestimation of the snow cover over boreal regions has been significantly reduced. Despite (or because of) this improved representation of snow, the model shows significant cold biases over the main mountains.

Regarding the representation of polar climates, the implementation of RRTM substantially improved the longwave radiative fluxes in the dry and cold polar atmosphere, reducing considerably the surface temperature biases over the ice sheet plateaus. While the distribution of liquid droplets and ice crystals in cold mixed phase clouds is closer to observations in LMDZ6, low-level clouds remain too abundant over high-latitude regions (Madeleine et al., manuscript 2020MS002046). The modifications of the subgrid turbulent scheme (Section 3.1) yielded more realistic temperature inversions over the Antarctic ice sheet. Overall, the representation of very stable polar boundary layers has been improved but the speed of katabatic winds remains underestimated over the coastal slopes of East Antarctica (Vignon et al., 2018). Over boreal continents, the new turbulent scheme allowed for more realistic near-surface temperatures, even though the prevailing warm bias in LMDZ5 (a classical bias in CMIP5, Wei et al., 2017) has been replaced by a pronounced cold bias over some regions like northern Canada (Cheruy et al., manuscript 2019MS002005). In forced mode, the sea ice representation in LMDZ6 remains simplistic and unchanged when compared to LMDZ5, with a constant sea ice thickness and thermal conductivity, and a sea ice albedo calculated only as a function of the snow cover fraction and snow age. This results in a cold surface temperature bias that was alleviated by reducing the default sea ice thickness in LMDZ6 (not shown). In coupled mode (Boucher et al., 2020), when using the comprehensive LIM3 module for sea ice, it turns out that the simulated near-surface winter temperature is too warm. A refined tuning of the subgrid scale orographic drag and lifting forces was also adopted to improve the representation of the Northern Hemisphere standing wave pattern. The resulting atmospheric heat transport toward the Arctic Ocean was subsequently reduced, thereby descreasing the winter warm bias (not shown). However over the Southern Ocean, LMDZ6 exhibits similar circulation biases as in LMDZ5, with, for instance, a strong anticyclonic bias over the Amundsen sea (Krinner et al. 2019).

5.4. Tropical Rainfall

We analyze more specifically in this section the tropical rainfall and its variability. The analyses are based on years 2000 to 2006 of the “amip” and “HighResMIP” simulations available on the CMIP5 and CMIP6 databases.

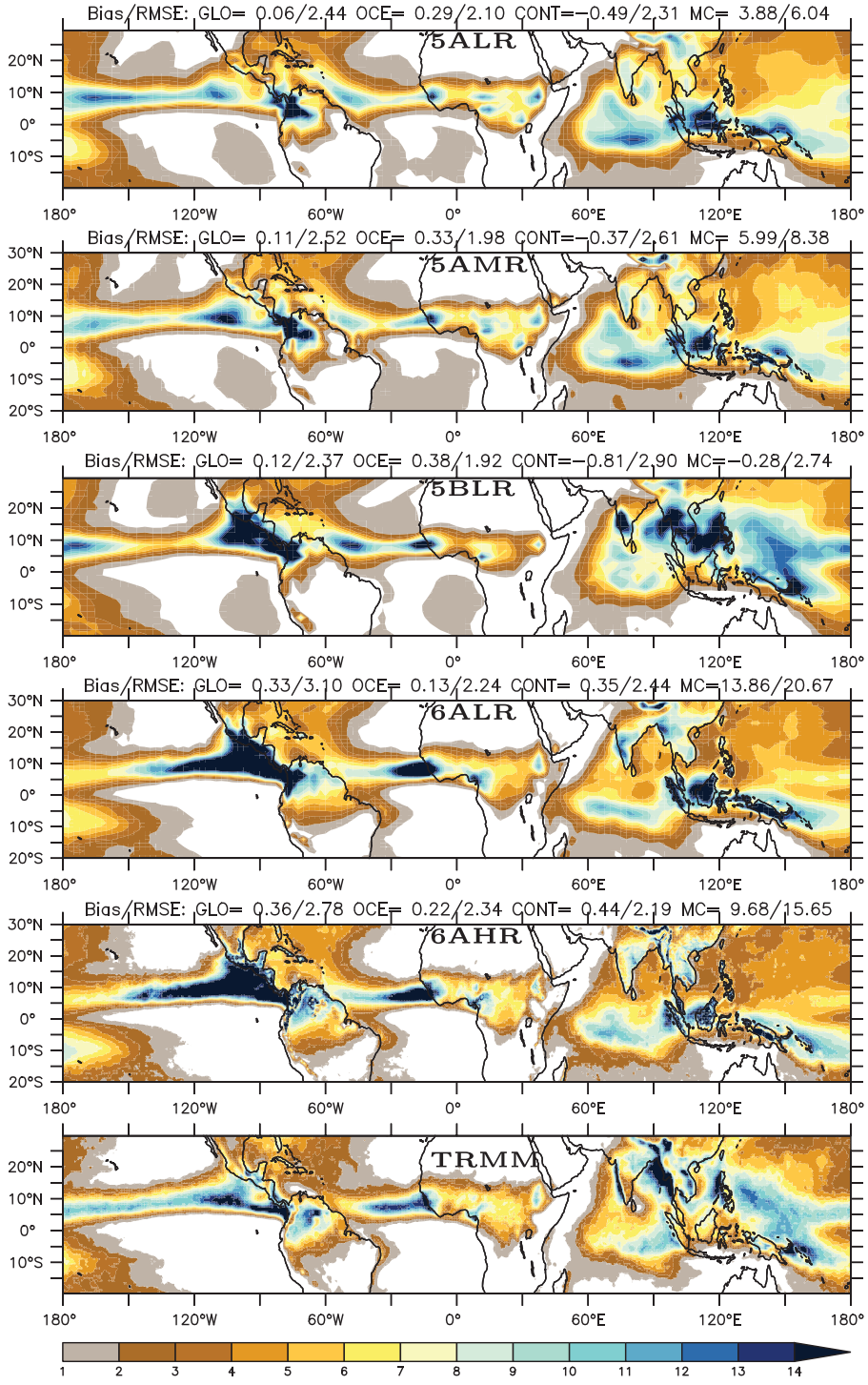

Figure 10. Average rainfall over the period June-July-August-September (mm/day, white if below 1 mm/day) for TRMM observations (top) and successive configurations of the model. The mean bias and root-mean-square errors (in mm/day) are shown on the top of each graph, considering either the full region (GLO), the Oceans only (OCE) or the continents, separating the Maritime continent (MC, defined by a box in longitude [90°E,180°E] and latitude [10°S,10°N]) from the other continents (CONT). Fields were interpolated on the LR^6 grid before computing the bias and root-mean-square error.

5.4.1. Seasonal Distribution

The discussion of rainfall seasonal distribution focuses on the monsoon season in the Northern Hemisphere. We show in Figure 10 the June-July-August-September (JJAS) mean rainfall.

One improvement of the 6A-LR and -HR simulations compared to previous versions is the reduction of the rainfall over East tropical oceans, identified in the 5A and 5B versions by the gray area with rainfall between 1 and 2 mm/day. This success in simulating almost no rainfall in these regions in the 6A version can be partly attributed to the modification of the thermal plume model for the representation of stratocumulus clouds, to the modification of the subcloud rainfall reevaporation described above, to the tuning of the parameters that control cloud microphysics and reevaporation but also to the new triggering formulation of the deep convection scheme which prevents deep convective rainfall to occur.

Rainfall is reinforced and is much too strong in the Pacific and Atlantic ITCZ, and globally over the ocean (as seen from the value of the mean bias at the top of each panel in Figure 10). This bias is particularly strong on the East part of the Pacific ITCZ and was not as strong in the previous versions.

On the contrary, the oceanic rainfall is much too weak north of the equator both over the Gulf of Bengal and over the warm pool in the West Pacific. In that respect, the deficiency of the 6A simulations is similar to that of the 5A version, while the 5B versions showed better skill. Together with this lack of rainfall over the ocean, rainfall is overly strong over the main islands of the maritime continent in the 5A and 6A simulations (see the MC bias at the top of each panel) while it was much weaker in the 5B versions. From a global perspective the mean rainfall was much better represented around the maritime continent in the 5B version.

One improvement of the 6A version concerns the West African monsoon. The agreement between the 6A-HR resolution simulation and TRMM observation is particularly impressive. The 6A-LR simulation is satisfactory in that respect as well and corrects a robust tendency of the previous versions, which were producing a too narrow band of rain in latitude with an underestimation over the Sahel, the semiarid band at the southern border of the Sahara. This deficiency, already present in the 5A version, was amplified in the 5B version. For the rainfall simulation over Sahel, both the modifications of the parameterizations and the tuning of model parameters are of importance. Consistently, the tendency of the model to underestimate rainfall at the northern limit of the Indian subcontinent is less pronounced in the 6A-LR than in the 5A versions, and less pronounced in the 5A than in the 5B version. The 6A-LR and -HR versions also represent the rainfall over the Amazon, which was strongly underestimated in the previous versions, much better.

Altogether, the representation of the rainfall is generally degraded over the oceanic ITCZ and improved over tropical continents and over the East tropical oceans. The seasonal cycle of rainfall is significantly improved in particular over the Amazon, Missisipi, and Congo basins. Increasing the resolution from LR to HR gives access to more details and improves in particular the rainfall distribution over South Asia, probably due in part to a better representation of the Himalaya barrier of synoptic disturbances that contributes for a large part to the rainfall over the plain of the Ganges as was identified with a zoomed version of LMDZ-5A by Krishnan et al. (2016).

5.4.2. Diurnal Cycle

The representation of the diurnal cycle of convection was one of the major improvements of the 5B version compared to 5A. The preconditioning of deep convection by a phase of shallow cumulus convection and the self-maintenance of deep convection through its interplay with cold pools are clearly responsible for a shift by several hours of the diurnal maximum of rainfall (Rio et al., 2009). There is in fact one fundamental difference between the standard (5A) and the new physical package (5B and 6A) that allows this shift in time: in the NP, the parameterizations of shallow convection, deep convection, and cold pools interplay by exchanging directly internal variables instead of being forced only by the instantaneous profiles of large-scale state variables (as is usually the case in classical parameterizations), thus letting an additional degree of freedom for the convection to develop. Despite further modifications in the convective parameterizations, the behavior of the 6A version is close to that of the 5B version, as seen in Figure 11 that compares the local time of the maximum of the first harmonic mode of the diurnal cycle of rainfall. This is thus a robust change with respect to SP versions that is observed in 1-D simulations of the diurnal cycle of deep convection over the continents, as well as in Rio et al. (2009).

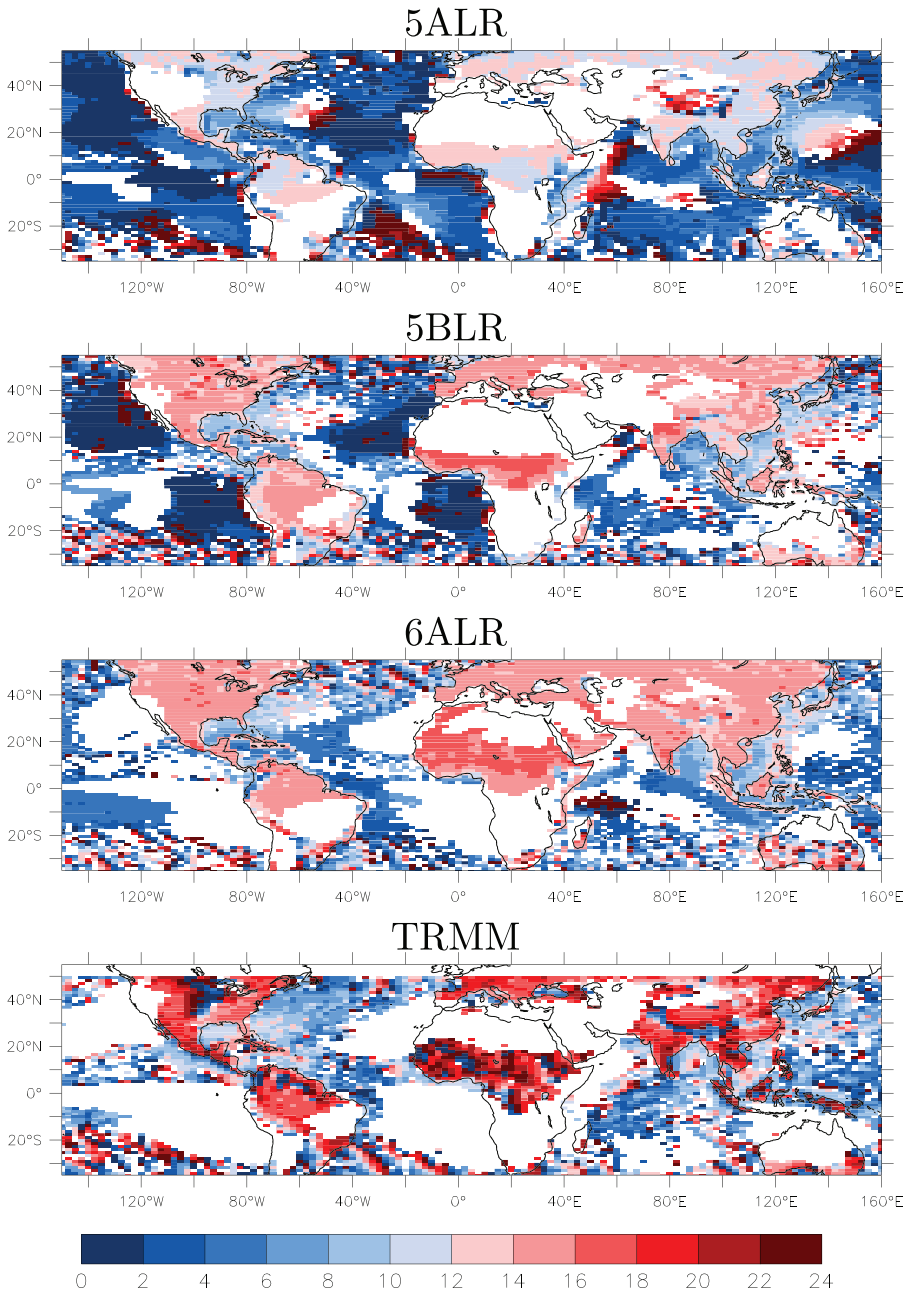

Figure 11. Observed and simulated time in the day of maximum rainfall computed as the phase of the first harmonic of the mean diurnal cycle for June-July-August. The white areas correspond to grid box where either the mean rainfall is smaller than 0.5 mm/day or the amplitude of the diurnal cycle is smaller than one fourth of the average rainfall at the same grid box.

Compared to TRMM observations, the convection occurs about 2 hr too early in the 6A version, typically between 14 and 16 LT instead of 16 to 18 LT on tropical continents, and specifically over Sahel, between 16 and 18 LT rather than 18 and 22 LT.

The lack of any representation of propagating systems in the model such as squall lines is a key reason for the remaining biases related to the timing and the location of precipitation in the tropics. This aspect is a long-standing topic of investigation in the model developer's community. Once this issue is solved, a great part of the so called “parameterization deadlock” might also be solved. Note that the propagation of convective systems away from mountains is responsible for the observed local night time (dark blue) maxima

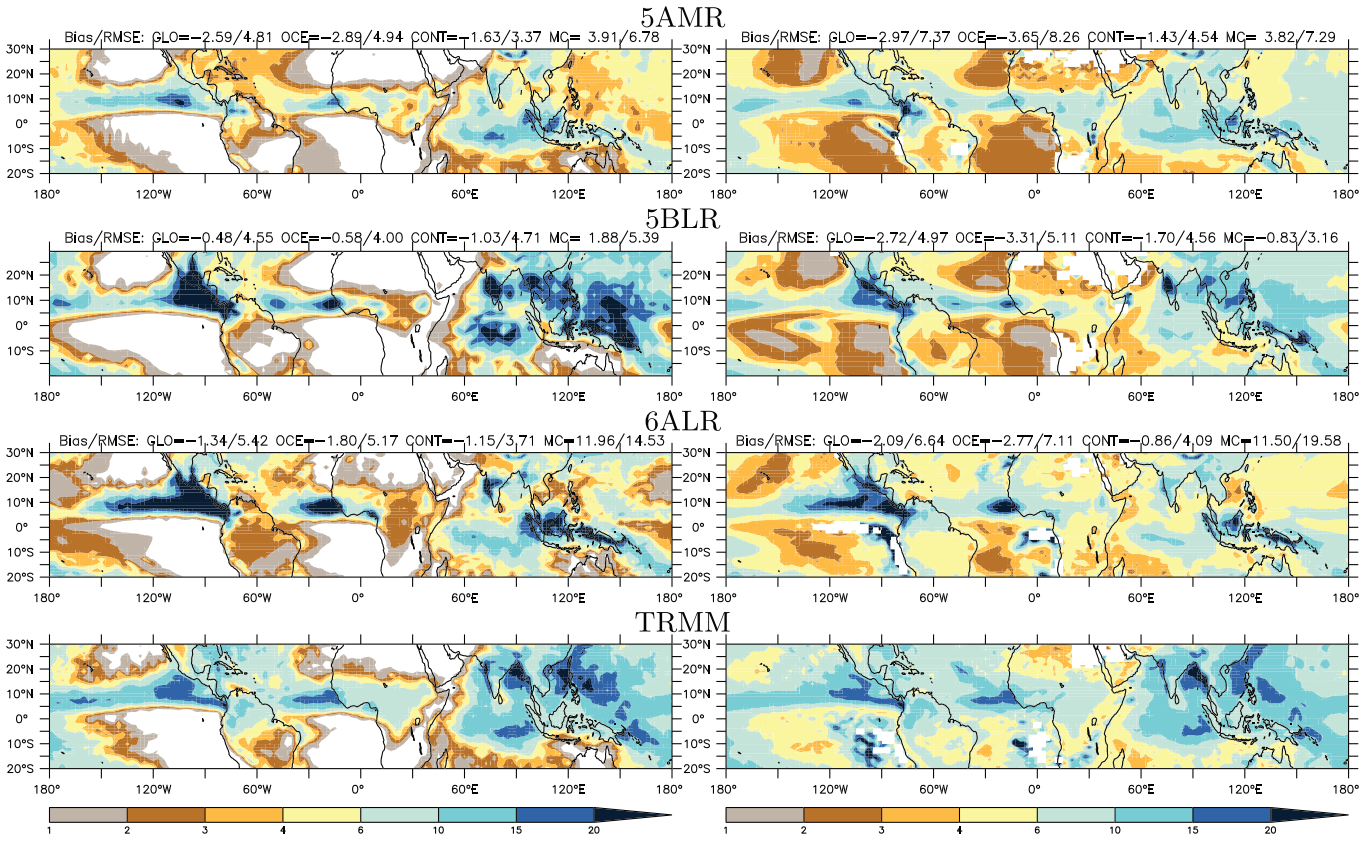

Figure 12. Rainfall variability for June-July-August-September for the 5A-LR^6 (top row), 5B-LR^6 (second row), 6A-LR simulation (third row), and TRMM observations (bottom row). (left) Standard deviation of the day-to-day variability (mm/day, white if smaller than 1 mm/day). (right) Average rainfall per day for the days with total rainfall larger than 1 mm (in mm/day, white if smaller than 1 mm/day). TRMM observations are interpolated on the LR^6 grid before computing statistics. The numbers given at the top of each graph are computed as in Figure 10.

of rainfall in central Sahel, over the U.S. great plains or in the southwest of France, where precipitation is known to initiate over mountains before propagating away.

Also note that the diurnal cycle is generally in phase with observations over the oceans (it was peaking earlier in the 5A version) with rainfall generally peaking between midnight and sunrise in the tropics and near noon offshore of the East Coast of USA and China. This result deserves further analysis.

5.4.3. Variability and Intermittency

We now concentrate on the day-to-day rainfall variability illustrated in Figure 12. The 5A version was showing very little of this variability (note that the 5A-LR^5 version, not shown, shows results almost identical to 6A-MR^5 or LR^6 shown here). The 5B version exhibits a much stronger variability. However, this variability is overestimated and corresponds for a large part to grid-scale numerical noise as discussed below.

Also note that for the 5A and 5B versions, the mean rainfall is related to too weak values of rainfall for the days with rain (larger than 1 mm) underlying the fact that it rains too often but with rainfall events which are not strong enough, as is often the case in large-scale models. The 6ALR version behaves much better over Sahel with respect to rainfall variability with rainfall above 6 mm per event, as seen in the observations. From a global point of view, the variability in this model version lies between that of the 5A and that of the 5B versions. The major deficiency of the 6A version is the very weak rainfall variability over the warm pool in the West Pacific north of the equator where the mean rainfall is underestimated as well. This is consistent with the fact that the Madden Julian Oscillation, the major mode of variability in the region, is not well captured (not shown). Note that in the same region, the much better representation of the mean rainfall in the 5B version was probably related to this overestimated day-to-day variability.

This problem is not solved by increasing the horizontal resolution, as shown in Figure 13. However, at this resolution, a particularly good agreement exists between model and observations over tropical continents

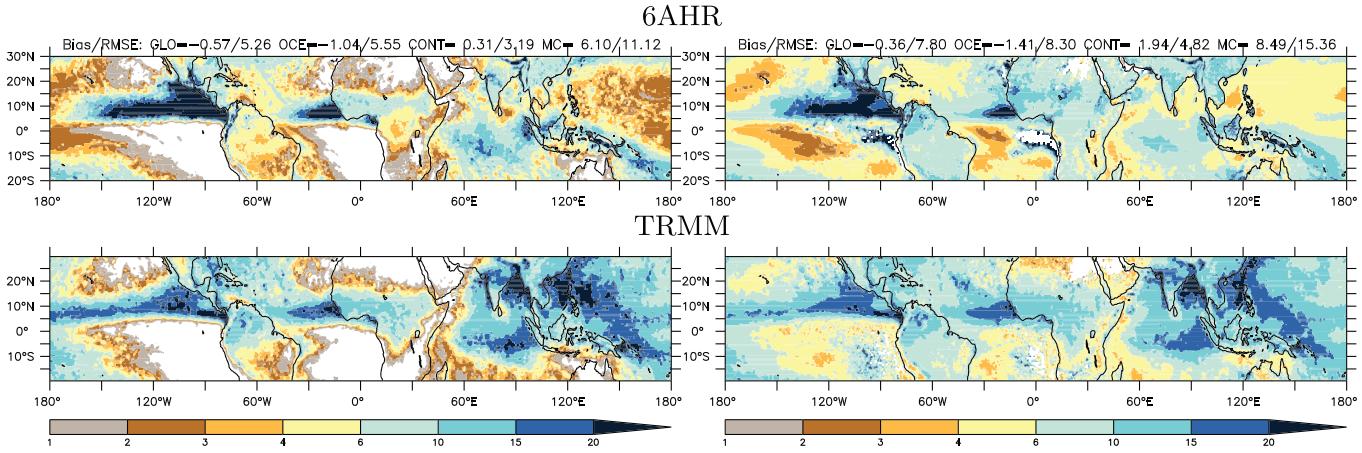

Figure 13. Rainfall variability for June-July-August-September for the 6A-HR configuration (top) and TRMM observations (bottom), showing on the left the standard deviation of the day-to-day variability (mm/day, white if smaller than 1 mm/day) and on the right the average rainfall per day for the days with total rainfall larger than 1 mm (in mm/day, white if smaller than 1 mm/day). TRMM observations are interpolated on the HR grid before computing statistics. The numbers given at the top of each graph are computed as in Figure 10.

in terms of rain intensity per rainfall event. The improvement is particularly strong over the Amazon basin and over Sahel.

The improvement in the intensity of rainfall events over the continents is a direct consequence of the implementation of the stochastic triggering. The stochastic triggering scheme has been specifically developed and tested over West Africa with the goal of better representing the observed day-to-day variability of rainfall very specific to these semiarid "transition regions" (Koster et al., 2004) in which the subtle coupling between the soil and the atmosphere is critical to decide whether or not the whole region may be in a dry or a moist state. In Rochetin et al. (2014b), some preliminary tests over the Sahelian region have clearly shown that intermittency of rainfall was significantly reinforced. The model was not only able to simulate the alternating between dry and rainy days, but it was also better in representing precipitation intensity variations during the monsoon season. Overall, the new stochastic triggering makes it more difficult for the deep convection scheme to be activated. The accumulation of CAPE in the atmosphere during dry days may be an explanation for these more irregular but more pronounced rainfall events.

5.4.4. Scale Awareness

As already mentioned, one major deficiency identified for the 5B version regarding the rainfall variability was to create strong rainfall at the grid scale. As a consequence, the apparent improvement from the 5A to 5B version associated with the increase of the day-to-day variability of rainfall was more an artifact than a real improvement. This behavior is illustrated in Figure 14 which shows the maximum rainfall intensity simulated and observed at a given latitude for a month of June. The TRMM observations correspond to June 2000. Because all the configurations were not available on the CMIP5 and CMIP6 databases, the results shown correspond to the first month of June of a simulation intitialized in January and run with climatological SSTs. This maximum rainfall intensity is typically of 200 to 300 mm in the TRMM data set (upper panel) and slightly increases if the observations are investigated with finer horizontal resolution: LR^6 (black), MR^6 (red), and HR^6 (green).

The 5B version is the worst version. It strongly overestimates rainfall even with the LR grid and leads to completely unrealistic daily rainfall, often larger than 1 m, at 50 km resolution. The 5A version produces reasonable extreme rainfall with the LR grid but extremes also increase too strongly when refining the grid.

The new 6A version produces a reasonable representation of both extreme rainfall and its increase with increasing grid resolution. This good behavior probably has several origins. The introduction of a proper iteration in the computation of the humidity at saturation for large-scale condensation seems to be a key aspect to reduce the frequency of grid point storms. The new stochastic triggering which targets scale awareness is probably an essential ingredient of the good representation of the sensitivity of the maximum rainfall to the horizontal grid resolution. Another important added value of the stochastic nature of the deep convection

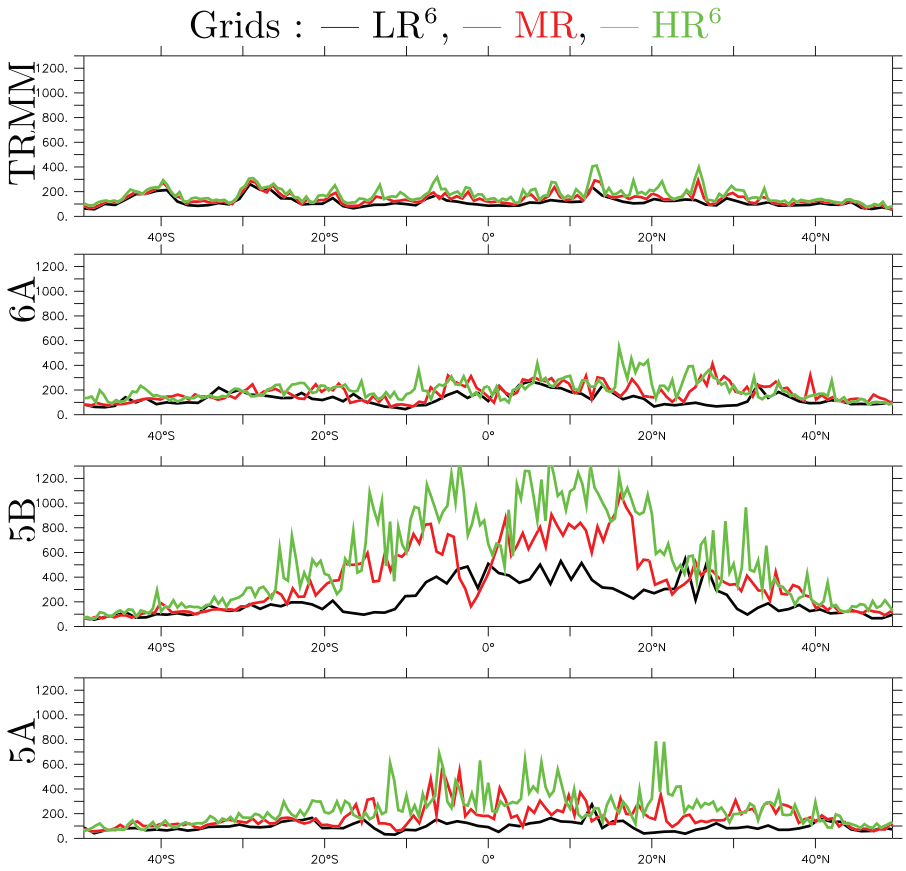

Figure 14. Maximum daily precipitation rate (mm/day) at a given latitude for the month of June, in atmospheric simulations forced by climatological SSTs. TRMM observations (top row) are compared with simulations with the various model physics: 6A (second row), 5B (third row), and 5A (bottom row). The results were shown for 1 month to avoid running HR simulations for the 5A and 5B versions, which will not be exploited beyond this particular diagnostic. The results (both for TRMM observations and simulations) are shown for the LR^6, MR^6, and HR^6 horizontal grid resolution. Because the 5A and 5B simulations were not available on the HR grid, all the simulations were rerun with the same recent source files of the LMDZ model.

triggering scheme is that it not only improves the day-to-day variability of rainfall but also almost guarantees the same spatial and temporal frequency of deep clouds regardless of the horizontal grid scale. Then, as predicted in Rochetin et al. (2014a), the stochastic component seems to provide some scale awareness to the model. Due to the important changes between 5B and 6A, this aspect deserves further investigation, for example, to better assess how far these changes are directly related to the new stochastic triggering.

6. Summary of Improvements, Shortcomings, and Development Pathways

The 6A version of the LMDZ model, which is the atmospheric component of the IPSL-CM6A version contributing to the CMIP6 exercise, is the result of a long model development. In particular, efforts were made to improve the physical content of the parameterizations that represent the turbulent, convective, and moist physics. In the new set of parameterizations, a unified view of the convective boundary layer is favored using the thermal plume model that combines a mass flux approach for boundary layer convection with eddy diffusion. For deep convection, the choice is to favor an object-oriented approach, in which deep convective clouds are coupled to cold pools and boundary layer organized circulation.

The early version 5B of this NP package suffered from a number of shortcomings.

The 6A version can be seen as the NP reaching maturity. In addition to major improvements such as the representation of stratocumulus without switching off the thermal plume mass flux model and the introduction of a stochastic triggering for deep convection, the tuning and evaluation were pushed much farther than for previous versions.

Compared to previous versions and also to the CMIP5 and CMIP6 multimodel ensemble for several aspects, the 6A version is characterized by the following:

1. An improved representation of the upper atmosphere, with, in particular, the presence of a quasi-biennial oscillation.
2. A reasonable and improved representation of CRE and radiation.
3. A better representation of stratocumulus and cumulus clouds.
4. A better representation of near surface turbulence, allowing in particular, for strong decoupling in very stable conditions.
5. A better representation of continental seasonal rainfall.
6. An improved and reasonable representation of rainfall diurnal cycle and intermittency.
7. A good behavior when increasing the resolution, with in particular a better representation of the details of rainfall climatology over the continents and a moderate increase in rainfall variability compatible with observations. This is an important result when addressing climate impact issues by downscaling the results of the global coarse grid coupled model with locally refined simulations using the zoom capability.

Not shown here, the classical summer warm biases over midlatitudes continents have also been significantly reduced compared to previous versions. Important cold biases persist over deserts (the Sahara in particular), which may be related to not accounting for the lower-than-unity thermal emissivity, or to aerosols specification or radiative properties. Cold biases have been reinforced and are strong over mountains, with, so far, no clear explanation as to why.

This general improvement was obtained thanks to both a long-term investigation of cloud processes and their parameterization, with intensive use of the SCM/LES comparison framework to inspire model developments and assess the validity of the developed parameterizations, and the rationalization of the development and tuning process. Altogether, it is a case where both the physics content of the model and some classical metrics like RMS error on seasonality of temperature or rainfall were improved.

It is worth mentioning some methodological aspects that we found helpful to reach this goal:

1. Introducing automatic quality control procedures like bit-to-bit comparison with previous versions when the modification was not expected to change the results (introduction of a diagnostic, optimization, etc.)
2. Ensuring backward compatibility to be able to rerun previous versions of the model with the latest source code, in order to understand, in particular, the cause of a degradation (sometimes identified several months or years afterward) of the model results on some particular aspect.
3. Systematic benchmarking of new configurations of the 3-D GCM on a series of 1-D test cases.
4. Using long series of multivariate observations on selected instrumented sites to be compared with nudged-by-wind simulations more systematically.
5. Rationalizing the tuning procedure with an explicitness of tuning targets and identification of specific targets for the stand-alone atmospheric model from coupled simulation.

It is noteworthy that a number of shortcomings were identified after freezing the model for CMIP6 simulations:

1. A bug was discovered in the computation of the 2 m temperature, which automatically created absurd values up to 500 K. The 2 m temperatures were corrected a posteriori in CMIP6 outputs (details given in Cheruy et al., manuscript 2019MS002005).
2. Following the modification of the boundary layer to allow strong near-surface decoupling, spurious oscillations of the surface temperature appeared, in particular over the Antarctic plateau. These oscillations are not just numerical noise since they are rather large-scale and resolved in time. Such oscillations were somehow already present in previous versions of the model, but they were masked or damped by the excessive turbulent mixing.
3. An effort was done to conserve energy better, and in particular the transformation of kinetic energy to heat by the convective and turbulent scheme. However, and despite significant efforts in that direction, the energy conservation with phase changes is still far from guaranteed. The final energy leak is of the order of a few tenths of W m^{-2} globally.

Beyond this, the main deficiencies identified so far for the new model version concern the rainfall distribution in the tropics over the oceans. The ITCZ is much too strong over the Pacific and the Atlantic Oceans,

Table A1
List of the CMIP5 Models Shown in Figure 6

Model	Group	SW CRE (W/m^2)	LW CRE (W/m^2)	TOT CRE (W/m^2)	OSR (W/m^2)	OLR (W/m^2)	PR (mm/day)
bcc-csm1-1-m	BCC	10.34(49)	4.77(41)	6.81(36)	7.42(39)	4.58(36)	0.44(6)
CanAM4	CCCma	2.89(3)	2.16(4)	3.21(4)	3.43(6)	1.34(1)	0.47(12)
CMCC-CM	CMCC	4.43(19)	1.65(1)	4.31(12)	6.46(29)	3.23(19)	0.54(23)
CNRM-CM5	CNRM-CERFACS	8.97(43)	5.74(46)	4.65(14)	8.24(46)	2.90(17)	0.64(44)
ACCESS1-0	CSIRO-BOM	4.37(18)	2.80(12)	5.39(22)	4.73(15)	5.33(46)	0.66(50)
ACCESS1-3		5.96(26)	2.31(7)	6.79(35)	5.64(25)	5.52(48)	0.73(57)
CSIRO-Mk3-6-0	CSIRO-QCCCE	6.87(34)	6.13(51)	12.09(53)	5.45(22)	5.32(45)	0.62(40)
inmcm4	INM	7.68(40)	7.33(54)	5.59(27)	3.70(9)	6.04(53)	0.90(60)
IPSL-CM5A-LR	IPSL	10.57(50)	5.84(47)	7.83(47)	10.19(52)	6.44(54)	0.45(7)
IPSL-CM5A-MR		10.23(48)	7.27(53)	7.16(38)	9.72(51)	6.84(55)	0.44(5)
IPSL-CM5B-LR		7.21(37)	2.83(13)	4.67(15)	7.07(36)	4.91(40)	0.41(3)
FGOALS-g2	LASG-CESS	6.97(35)	3.88(32)	8.00(49)	7.71(42)	3.93(29)	0.63(43)
FGOALS-s2	LASG-IAP	6.66(31)	9.22(57)	12.85(56)	9.50(49)	6.04(52)	0.65(48)
MIROC5	MIROC	13.46(56)	3.43(24)	12.43(54)	12.00(57)	4.99(42)	0.83(58)
MIROC-ESM		10.68(51)	3.50(26)	12.54(55)	11.28(55)	3.34(21)	0.51(18)
HadGEM2-A	MOHC	4.56(21)	2.93(16)	5.27(21)	5.09(19)	5.08(43)	0.65(47)
MPI-ESM-LR	MPI-M	6.44(29)	2.87(14)	5.46(24)	6.79(33)	5.53(49)	0.56(28)
MPI-ESM-MR		7.26(38)	4.06(33)	5.57(26)	6.68(32)	5.62(50)	0.60(34)
MRI-AGCM3-2H	MRI	9.74(47)	3.19(20)	7.41(42)	8.53(47)	2.48(10)	0.53(20)
MRI-AGCM3-2S		9.05(44)	3.60(28)	7.03(37)	7.03(35)	3.69(26)	0.60(35)
MRI-CGCM3		9.21(45)	5.60(45)	5.86(30)	11.63(56)	4.61(37)	0.56(26)
GISS-E2-R	NASA-GISS	12.60(53)	8.31(56)	13.73(57)	9.63(50)	3.67(25)	0.85(59)
CCSM4	NCAR	9.71(46)	4.82(43)	6.79(34)	9.29(48)	3.78(27)	0.64(45)
NorESM1-M	NCC	12.70(54)	6.11(50)	7.27(39)	10.45(54)	7.29(56)	0.62(41)
GFDL-CM3	NOAA-GFDL	3.61(6)	4.39(36)	4.74(19)	5.84(26)	5.51(47)	0.70(55)
GFDL-HIRAM-C180		5.20(24)	1.89(2)	5.99(31)	7.67(40)	4.97(41)	0.58(31)
GFDL-HIRAM-C360		4.23(14)	2.25(6)	5.78(29)	6.20(28)	3.91(28)	0.61(36)
CESM1-CAM5	NSF-DOE-NCAR	8.01(42)	6.14(52)	9.97(51)	7.31(38)	1.72(5)	0.69(53)

Note. The second column shows the name of the corresponing institution or team. The numbers given in the following columns correspond to the RMS error on the zonal mean (RMSz in Figure 6) and corresponding ranking within parenthesis. The six columns correspond to the six panels of the figure.

and much too weak north of the equator over the ocean surrounding the maritime continent. The precipitation is also much too large on the islands and on the maritime continent. The day-to-day and intraseasonal variability of the tropical rainfall is underestimated as well over ocean in that region, while it was represented fairly well in the 5B version. The Madden Julian Oscillation is not captured well by the model either; the intraseasonal variability which is already too weak over the Indian tropical ocean is not able to propagate across the maritime continent (not shown). The seasonality of ENSO events is not well captured either by the coupled model (Boucher et al., 2020).

No real path has been identified so far to solve these issues in the 6A version of the model. Some important physical processes are probably still misrepresented in the model, such as high-level clouds associated with deep convection, heat, and momentum transport associated with mesoscale circulations – shown to impact large-scale patterns of precipitation (Moncrieff, 2019)—or the impact of land-sea breezes on convection. These developments will be targeted in the future. Being able to simultaneously tune the radiative forcing (as was done quite systematically here) and the representation of convective rainfall is probably a key issue. This will be possible only if applying more systematic methodologies to the tuning process. We recently started to use the history matching approach (Williamson et al., 2013) in which the range of acceptable parameters is iteratively reduced to match some predefined metrics. This is achieved by making use of emulators or

Table A2
Same as Table A1 but for CMIP6 Models

Model	Group	SW CRE (W/m^2)	LW CRE (W/m^2)	TOT CRE (W/m^2)	OSR (W/m^2)	OLR (W/m^2)	PR (mm/day)
BCC-CSM2-MR	BCC	7.12(36)	2.56(9)	6.43(32)	7.17(37)	2.59(13)	0.59(33)
BCC-ESM1		11.36(52)	4.56(40)	7.99(48)	7.83(44)	7.81(57)	0.47(9)
CAMS-CSM1-0	CAMS	4.05(9)	2.95(18)	3.80(9)	6.93(34)	4.49(34)	0.46(8)
FGOALS-f3-L	CAS	6.06(27)	8.12(55)	6.46(33)	5.26(20)	4.39(33)	0.54(22)
FGOALS-g3		4.94(22)	2.90(15)	2.81(3)	6.15(27)	5.19(44)	0.44(4)
CanESM5	CCCma	3.27(4)	2.62(10)	2.74(2)	2.78(4)	1.70(4)	0.56(25)
CNRM-CM6-1	CNRM-CERFACS	6.42(28)	4.30(35)	7.81(46)	6.61(31)	2.58(12)	0.53(21)
CNRM-ESM2-1		6.49(30)	4.18(34)	7.38(41)	6.60(30)	2.37(7)	0.52(19)
E3SM-1-0	E3SM-Project	4.45(20)	2.94(17)	4.77(20)	3.62(7)	2.89(16)	0.58(32)
EC-Earth3	EC-Earth-Consortium	6.69(33)	2.18(5)	7.43(44)	7.92(45)	2.48(9)	0.48(11)
EC-Earth3-Veg		6.66(32)	2.12(3)	7.42(43)	7.80(43)	2.45(8)	0.47(10)
IPSL-CM6A-HR	IPSL	4.35(17)	3.45(25)	4.71(17)	4.64(14)	2.50(11)	0.62(39)
IPSL-CM6A-LR		3.76(7)	2.66(11)	4.08(10)	4.74(16)	2.94(18)	0.61(37)
MIROC6	MIROC	14.07(57)	3.61(29)	11.86(52)	13.14(58)	9.94(58)	0.72(56)
HadGEM3-GC31-LL	MOHC	4.13(13)	4.51(39)	3.65(7)	3.64(8)	4.04(31)	0.66(51)
HadGEM3-GC31-MM		4.94(23)	4.88(44)	3.38(5)	3.93(10)	4.21(32)	0.68(52)
UKESM1-0-LL		4.29(16)	4.81(42)	3.76(8)	4.00(11)	4.01(30)	0.64(46)
MRI-ESM2-0	MRI	4.08(10)	2.96(19)	2.57(1)	2.67(3)	1.81(6)	0.57(30)
GISS-E2-1-G	NASA-GISS	7.40(39)	5.88(49)	9.46(50)	5.46(23)	3.64(23)	0.57(29)
CESM2	NCAR	3.56(5)	3.55(27)	4.68(16)	4.07(12)	2.71(15)	0.41(2)
CESM2-WACCM		3.80(8)	3.25(21)	4.71(18)	4.16(13)	3.29(20)	0.41(1)
NorCPM1	NCC	12.80(55)	5.86(48)	7.72(45)	10.37(53)	5.69(51)	0.63(42)
NorESM2-LM		4.11(11)	3.80(31)	5.39(23)	5.06(18)	4.62(38)	0.49(15)
GFDL-AM4	NOAA-GFDL	2.04(2)	3.25(22)	4.55(13)	2.37(1)	1.64(3)	0.50(17)
GFDL-CM4		1.83(1)	3.27(23)	4.31(11)	2.52(2)	1.44(2)	0.49(14)
NESM3	NUIST	4.12(12)	2.34(8)	3.48(6)	5.05(17)	4.72(39)	0.49(13)
SAM0-UNICON	SNU	4.26(15)	4.48(38)	5.61(28)	3.29(5)	2.65(14)	0.65(49)

metamodels, based on a reasonable sample of a few hundreds of global simulations, to compute metrics in the full space of parameters (up to a few tens of dimensions)

Appendix A: Details About CMIP Models Analyzed in Figure 6

To help read Figure 6, we give the names of the models, together with the corresponding institutions and numerical values displayed in the figure in two tables: Table A1 for CMIP5 models and Table A1 for CMIP6 models.

Acknowledgments
This work received funding from Grant HIGH-TUNE ANR-16-CE01-0010. It was supported by the DEPHY2 project funded by the French national program LEFE/INSU. The 3-D simulations were granted access to the HPC resources of IDRIS and TGCC under the allocation gencmip6 attributed by GENCI (Grand Equipement National de Calcul Intensif). This study benefited from the ESPRI computing and data center (https://mesocentre.ipsl.fr), which is supported by CNRS, Sorbonne Université, Ecole Polytechnique, and CNES as well as through national and international grants. It also benefited from the "Convergence" ANR project (grant# ANR-13-MONU-0008). The last version of the LMDZ source code can be downloaded freely from the LMDZ web site. The version used for the specific simulation runs for this paper is the “svn” release 3404 from 16 October 2018, which can be downloaded and installed on a Linux computer by running the “install_lmdz.sh” script available at this site (http://www.lmd.jussieu.fr/~/pub:./install_lmdz.sh.-v20181016.trunk). A large part of the outputs used is archived on the CMIP5 and CMIP6 archives, distributed through the Earth System Grid Federation (ESGF) and freely accessible through the ESGF data portals after registration. Details about ESGF are presented on the CMIP Panel website (http://www.wcrp-climate.org/index.php/wgcm-cmip/about-cmip). Preprocessed files will be made available with a DOI if the paper is accepted for publication, together with the scripts used to generate the figures.

References

Arakawa, A., & Wu, C. M. (2013). A unified representation of deep moist convection in numerical modeling of the atmosphere. Part I. *Journal of the Atmospheric Sciences*, *70*, 1977–1992. https://doi.org/10.1175/JAS-D-12-0330.1

Bazile, E., Couvreux, F., Le Moigne, P., Genthon, C., Holtslag, A. A. M., & Svensson, G. (2014). GABLS4: An intercomparison case to study the stable boundary layer over the Antarctic plateau. *GEWEX News*, *24*, 4.

Berg, W., L'Ecuyer, T., & Haynes, J. M. (2010). The distribution of rainfall over oceans from spaceborne radars. *Journal of Applied Meteorology and Climatology*, *49*(3), 535–543. https://doi.org/10.1175/2009JAMC2330.1

Bertrand, T., & Forget, F. (2016). Observed glacier and volatile distribution on Pluto from atmosphere-topography processes. *Nature*, *540*, 86–89. https://doi.org/10.1038/nature19337

Bony, S., & Emanuel, K. A. (2001). A parameterization of the cloudiness associated with cumulus convection; evaluation using TOGA COARE data. *Journal of Atmospheric Sciences*, *58*, 3158–3183.

Boone, A., & Etchevers, P. (2001). An intercomparison of three snow schemes of varying complexity coupled to the same land surface model: Local-scale evaluation at an alpine site. *Journal of Hydrometeorology*, *2*(4), 374–394. https://doi.org/10.1175/1525-7541(2001)002<0374:AIOTSS>2.0.CO;2

Boucher, O., & Lohmann, U. (1995). The sulfate-CCN-cloud albedo effect. *Tellus Series B Chemical and Physical Meteorology B*, *47*(3), 281. https://doi.org/10.3402/tellusb.v47i3.16048

Boucher, O., Servonnat, J., Albright, A. L., Aumont, O., Balkanski, Y., Bastrikov, V., et al. (2020). Presentation and evaluation of the IPSLCM6ALR climate model. *Journal of Advances in Modeling Earth Systems*, *12*, e2019MS002010. https://doi.org/10.1029/2019MS002010

Brown, A., Cederwall, R., Chlond, A., Duynkerke, P., Golaz, J. C., Khairoutdinov, M., & Stevens, B. (2002). Large-eddy simulation of the diurnal cycle of shallow cumulus convection over land. *Quarterly Journal of the Royal Meteorological Society*, *128*, 1075–1093.

Chatfield, R. B., & Brost, R. A. (1987). A two-stream model of the vertical transport of trace species in the convective boundary layer. *Journal of Geophysical Research*, *92*, 13,263–13,276.

Codron, F. (2012). Ekman heat transport for slab oceans. *Climate Dynamics*, *38*(1-2), 379–389. https://doi.org/10.1007/s00382-011-1031-3

Coindreau, O., Hourdin, F., Haeffelin, M., Mathieu, A., & Rio, C. (2007). Assessment of physical parameterizations using a global climate model with stretchable grid and nudging. *Monthly Weather Review*, *135*, 1474–1489. https://doi.org/10.1175/MWR3338.1

D'Orgeval, T., Polcher, J., & de Rosnay, P. (2008). Sensitivity of the West African hydrological cycle in ORCHIDEE to infiltration processes. *Hydrology and Earth System Sciences*, *12*(6), 1387–1401.

da Silva, A., Young, A. C., & Levitus, C. (1994). Atlas of surface marine data 1994, volume 1.: Algorithms and procedures. 6, U.S. Department of Commerce, NOAA, NESDIS.

De Rosnay, P., Polcher, J., Bruen, M., & Laval, K. (2002). Impact of a physically based soil water flow and soil-plant interaction representation for modeling large-scale land surface processes. *Journal of Geophysical Research*, *107*(D11), 4118. https://doi.org/10.1029/2001JD000634

de la Cámara, A., & Lott, F. (2015). A stochastic parameterization of the gravity waves emitted by fronts and jets. *Geophysical Research Letters*, *42*, 2071–2078. https://doi.org/10.1002/GL063298

de la Cámara, A., Lott, F., & Abalos, M. (2016). Climatology of the middle atmosphere in LMDz: Impact of source-related parameterizations of gravity wave drag. *Journal of Advance in Modeling Earth Systems*, *8*, 1507–1525. https://doi.org/10.1002/2016MS000753

Deardorff, J. W. (1966). The counter-gradient heat-flux in the lower atmosphere and in the laboratory. *Journal of Atmospheric Sciences*, *23*, 503–506.

Dee, D. P., Uppala, S. M., Simmons, A. J., Berrisford, P., Poli, P., Kobayashi, S., & Vitart, F. (2011). The ERA-Interim reanalysis: Configuration and performance of the data assimilation system. *Quarterly Journal of the Royal Meteorological Society*, *137*, 553–597. https://doi.org/10.1002/qj.828

Diallo, F. B., Hourdin, F., Rio, C., Traore, A. K., Mellul, L., Guichard, F., & Kergoat, L. (2017). The surface energy budget computed at the grid-scale of a climate model challenged by station data in West Africa. *Journal of Advance in Modeling Earth Systems*, *9*, 2710–2738. https://doi.org/10.1002/2017MS001081

Dufresne, J. L., Foujols, M. A., Denvil, S., Caubel, A., Marti, O., Aumont, O., & Vuichard, N. (2013). Climate change projections using the IPSL-CM5 Earth System Model: From CMIP3 to CMIP5. *Climate Dynamics*, *40*, 2123–2165. https://doi.org/10.1007/s00382-012-1636-1

Emanuel, K. A. (1991). A scheme for representing cumulus convection in large-scale models. *Journal of Atmospheric Sciences*, *48*, 2313–2335.

Gentine, P., Pritchard, M., Rasp, S., Reinaudi, G., & Yacalis, G. (2018). Could machine learning break the convection parameterization deadlock? *Geophysical Research Letters*, *45*, 5742–5751. https://doi.org/10.1029/2018GL078202

Grandpeix, J., & Lafore, J. (2010). A density current parameterization coupled with emanuel's convection scheme. Part I: The models. *Journal of Atmospheric Sciences*, *67*, 881–897. https://doi.org/10.1175/2009JAS3044.1

Grandpeix, J., Lafore, J., & Cheruy, F. (2010). A density current parameterization coupled with Emanuel's convection scheme. Part II: 1D simulations. *Journal of Atmospheric Sciences*, *67*, 898–922. https://doi.org/10.1175/2009JAS3045.1

Grandpeix, J. Y., Phillips, V., & Tailleux, R. (2004). Improved mixing representation in Emanuel's convection scheme. *Quarterly Journal of the Royal Meteorological Society*, *130*, 3207–3222.

Guichard, F., & Mongon, S. (2000). A parameterization of mesoscale enhancement of surface fluxes for large scale models. *Journal Climate*, *13*, 402–421.

Heymsfield, A. J. (1986). Ice particles observed in a cirriform cloud at −83 °C and implications for polar stratospheric clouds. *Journal of Atmospheric Sciences*, *43*(8), 851–856. https://doi.org/10.1175/1520-0469(1986)043<0851:IPOIAC>2.0.CO;2

Hines, C. O. (1997). Doppler-spread parameterization of gravity-wave momentum deposition in the middle atmosphere. Part 2: Broad and quasi monochromatic spectra, and implementation. *Journal of Atmospheric and Solar-Terrestrial Physical*, *59*(4), 387–400.

Holtslag, A. A. M., Svensson, G., Baas, P., Basu, S., Beare, B., Beljaars, A. C. M., & Van de Wiel, B. J. H. (2013). Stable boundary layers and diurnal cycles. *Bulletin of the American Mathematical Society*, *94*, 1691–1706. https://doi.org/10.1175/BAMS-D-11-00187.1

Hourdin, F., Couvreux, F., & Menut, L. (2002). Parameterisation of the dry convective boundary layer based on a mass flux representation of thermals. *Journal of the Atmospheric Sciences*, *59*, 1105–1123.

Hourdin, F., Foujols, M. A., Codron, F., Guemas, V., Dufresne, J. L., Bony, S., & Bopp, L. (2013). Impact of the LMDZ atmospheric grid configuration on the climate and sensitivity of the IPSL-CM5A coupled model. *Climate Dynamics*, *40*, 2167–2192. https://doi.org/10.1007/s00382-012-1411-3

Hourdin, F., Găinusă-Bogdan, A., Braconnot, P., Dufresne, J. L., Traore, A. K., & Rio, C. (2015). Air moisture control on ocean surface temperature, hidden key to the warm bias enigma. *Geophysical Research Letters*, *42*, 10,885–10,893. https://doi.org/10.1002/2015GL066764

Hourdin, F., Grandpeix, J. Y., Rio, C., Bony, S., Jam, A., Cheruy, F., & Roehrig, R. (2013). LMDZ5B: the atmospheric component of the IPSL climate model with revisited parameterizations for clouds and convection. *Climate Dynamics*, *40*, 2193–2222. https://doi.org/10.1007/s00382-012-1343-y

Hourdin, F., Jam, A., Rio, C., Couvreux, F., Sandu, I., Lefebvre, M. P., & Idelkadi, A. (2019). Unified parameterization of convective boundary layer transport and clouds with the thermal plume model. Accepted in JAMES.

Hourdin, F., Mauritsen, T., Gettelman, A., Golaz, J. C., Balaji, V., Duan, Q., & Williamson, D. (2017). The art and science of climate model tuning. *Bulletin of the American Meteorological Society*, *98*, 589–602. https://doi.org/10.1175/BAMS-D-15-00135.1

Hourdin, F., Musat, I., Bony, S., Braconnot, P., Codron, F., Dufresne, J. L., & Lott, F. (2006). The LMDZ4 general circulation model: Climate performance and sensitivity to parametrized physics with emphasis on tropical convection. *Climate Dynamics*, *27*, 787–813. https://doi.org/10.1007/s00382-006-0158-0

Hourdin, F., Rio, C., Jam, A., Traore, A. K., & Musat, I. (2019). Convective boundary layer control of the sea surface temperature in the tropics.

Huffman, G. J., Adler, R. F., Morrissey, M. M., Bolvin, D. T., Curtis, S., Joyce, R., & Susskind, J. (2001). Global precipitation at one-degree daily resolution from multisatellite observations. *Journal of Hydrometeorology*, *2*, 36–50. https://doi.org/10.1175/1525-7541(2001)002<0036:GPAODD>2.0.CO;2

Iacobellis, S. F., & Somerville, R. C. J. (2000). Implications of microphysics for cloud-radiation parameterizations: Lessons from TOGA COARE. *Journal of Atmospheric Sciences*, *57*(2), 161–183. https://doi.org/10.1175/1520-0469(2000)057<0161:IOMFCR>2.0.CO;2

Jam, A. (2012). Paramétrisation de la couche limite: Du modèle des thermiques au modèle statistique de nuage (PhD thesis), advized by Hourdin, Frédéric, Sciences de l'environnement, Paris 6 2012, 2012PA066672. https://www.theses.fr/2012PA066672

Jam, A., Hourdin, F., Rio, C., & Couvreux, F. (2013). Resolved versus parametrized boundary-layer plumes. Part III: Derivation of a statistical scheme for cumulus clouds. *Boundary-layer Meteorology*, *147*, 421–441. https://doi.org/10.1007/s10546-012-9789-3

Jouhaud, J., Dufresne, J. L., Madeleine, J. B., Hourdin, F., Couvreux, F., Villefranque, N., & Jam, A. (2018). Accounting for vertical subgrid-scale heterogeneity in low-level cloud fraction parameterizations. *Journal of Advance in Modeling Earth Systems*, *10*, 2686–2705. https://doi.org/10.1029/2018MS001379

Kasahara, A. (1977). Computational aspects of numerical models for weather prediction and climate simulation. In J. Chang (Ed.), *General circulation models of the atmosphere*, Methods in computational physics: Advances in research and applications (Vol. 17, pp. 1–66) . Elsevier. ISSN: 0076-6860. https://doi.org/10.1016/B978-0-12-460817-7.50006-9

Kato, S., Rose, F. G., Sun-Mack, S., Miller, W. F., Chen, Y., Rutan, D. A., & Collins, W. D. (2011). Improvements of top-of-atmosphere and surface irradiance computations with CALIPSO-, CloudSat-, and MODIS-derived cloud and aerosol properties. *Journal of Geophysical Research*, *116*, D19209. https://doi.org/10.1029/2011JD016050

Khairoutdinov, M., Randall, D., & Demott, C. (2005). Simulations of the atmospheric general circulation using a cloud-resolving model as a superparameterization of physical processes. *Journal of Atmospheric Sciences*, *62*, 2136–2154. https://doi.org/10.1175/JAS3453.1

King, J. C., Connolley, W. M., & Derbyshire, S. H. (2001). Sensitivity of modelled Antarctic climate to surface and boundary-layer flux parametrizations. *Quarterly Journal of the Royal Meteorological Society*, *127*, 779–794.

Kooperman, G. J., Pritchard, M. S., Burt, M. A., Branson, M. D., & Randall, D. A. (2016). Impacts of cloud superparameterization on projected daily rainfall intensity climate changes in multiple versions of the Community Earth System Model. *Journal of Advance in Modeling Earth Systems*, *8*, 1727–1750. https://doi.org/10.1002/2016MS000715

Koster, R. D., Dirmeyer, P. A., Guo, Z., Bonan, G., Chan, E., Cox, P., & Yamada, T. (2004). Regions of strong coupling between soil moisture and precipitation. *Science*, *305*(5687), 1138–1141. https://doi.org/10.1126/science.1100217

Krishnan, R., Sabin, T. P., Vellore, R., Mujumdar, M., Sanjay, J., Goswami, B. N., & Terray, P. (2016). Deciphering the desiccation trend of the South Asian monsoon hydroclimate in a warming world. *Climate Dynamics*, *47*, 1007–1027. https://doi.org/10.1007/s00382-015-2886-5

L'Hévéder, B., Codron, F., & Ghil, M. (2015). Impact of anomalous northward oceanic heat transport on global climate in a slab ocean setting. *Journal Climate*, *28*(7), 2650–2664. https://doi.org/10.1175/JCLI-D-14-00377.1

Lac, C., Chaboureau, J. P., Masson, V., Pinty, J. P., Tulet, P., Escobar, J., & Wautelet, P. (2018). Overview of the Meso-NH model version 5.4 and its applications. *Geoscience Model Development*, *11*, 1929–1969. https://doi.org/10.5194/gmd-11-1929-2018

Lafore, J. P., Stein, J., Asencio, N., Bougeault, P., Ducrocq, V., Duron, J., & Vil-Guerau de Arellano, J. (1998). The Meso-NH atmospheric simulation system. Part I: Adiabatic formulation and control simulations. *Annales Geophysicae*, *6*, 90–109.

Laval, K., Sadourny, R., & Serafini, Y. (1981). Land surface processes in a simplified general circulation model. *Geophysical Astrophysical Fluid Dynamics*, *17*, 129–150.

Lebonnois, S., Burgalat, J., Rannou, P., & Charnay, B. (2012). Titan global climate model: New 3-dimensional version of the IPSL Titan GCM. *Icarus*, *218*, 707–722. https://doi.org/10.1016/j.icarus.2011.11.032

Li, F., Rosa, D., Collins, W. D., & Wehner, M. F. (2012). "Super-parameterization": A better way to simulate regional extreme precipitation? *Journal of Advance in Modeling Earth Systems*, *4*, M4002. https://doi.org/10.1029/2011MS000106

Loeb, N. G., Wielicki, B. A., Doelling, D. R., Smith, G. L., Keyes, D. F., Kato, S., & Wong, T. (2009). Toward optimal closure of the Earth's top-of-atmosphere radiation budget. *Journal Climate*, *22*(3), 748–766. https://doi.org/10.1175/2008JCLI2637.1

Lott, F. (1999). Alleviation of stationary biases in a GCM through a mountain drag parameterization scheme and a simple representation of mountain lift forces. *Monthly Weather Review*, *127*, 788–801. https://doi.org/10.1175/1520-0493(1999)127<0788:AOSBIA>2.0.CO;2

Lott, F., Fairhead, L., Hourdin, F., & Levan, P. (2005). The stratospheric version of LMDz: Dynamical climatologies, Arctic oscillation, and impact on the surface climate. *Climate Dynamics*, *25*, 851–868. https://doi.org/10.1007/s00382-005-0064-x

Lott, F., & Guez, L. (2013). A stochastic parameterization of the gravity waves due to convection and its impact on the equatorial stratosphere. *Journal of Geophysical Research: Atmospheres*, *118*, 8897–8909. https://doi.org/10.1002/jgrd.50705

Louis, J. F. (1979). A parametric model of vertical eddy fluxes in the atmosphere. *Boundary-layer Meteorology*, *17*, 187–202.

Louis, J. F., Tiedtke, M., & Geleyn, J. F. (1982). A short history of the operational pbl parametrization at ECMWF. Paper presented at the ECMWF workshop on boundary layer parametrization, ECMWF, Reading.

Lurton, T., Balkanski, Y., Bastrikov, V., Bekki, S., Bopp, L., Braconnot, P., et al. (2020). Implementation of the CMIP6 forcingdata in the IPSL-CM6A-LR model. *Journal of Advances in Modeling Earth Systems*, *12*, e2019MS001940. https://doi.org/10.1029/2019MS001940

Madec, G., Bourdallé-Badie, R., Bouttier, P., Bricaud, C., Bruciaferri, D., Calvert, D., & Vancoppenolle, M. (2017). NEMO ocean engine (Version v3.6). Notes du Ple de modélisation de l'Institut Pierre-simon Laplace (IPSL), https://doi.org/10.5281/zenodo.1472492

Mlawer, E. J., Taubman, S. J., Brown, P. D., Iacono, M. J., & Clough, S. A. (1997). Radiative transfer for inhomogeneous atmospheres: RRTM, a validated correlated-k model for the longwave. *Journal of Geophysical Research*, *102*(D14), 16,663–16,682. https://doi.org/10.1029/97JD00237

Moncrieff, M. W. (2019). Toward a dynamical foundation for organized convection parameterization in GCMs. *Geophysical Research Letters*, *46*, 14,103–14,108. https://doi.org/10.1029/2019GL085316

Morcrette, J. (1991). Radiation and cloud radiative properties in the European Centre for Medium Range Weather Forecasts forecasting system. *Journal of Geophysical Research*, *96*, 9121–9132.

Navarro, T., Schubert, G., & Lebonnois, S. (2018). Atmospheric mountain wave generation on Venus and its influence on the solid planet's rotation rate. *Nature Geoscience*, *11*, 487–491. https://doi.org/10.1038/s41561-018-0157-x

Park, S. (2014). A unified convection scheme (UNICON). Part I: Formulation. *Journal of Atmospheric Sciences*, *71*, 3902–3930. https://doi.org/10.1175/JAS-D-13-0233.1

Randall, D., Khairoutdinov, M., Arakawa, A., & Grabowski, W. (2003). Breaking the cloud parameterization deadlock. *Bulletin of the American Meteorological Society*, *84*, 1547–1564. https://doi.org/10.1175/BAMS-84-11-1547

Rio, C., Del Genio, A. D., & Hourdin, F. (2019). Ongoing breakthroughs in convective parameterization. *Current Climate Change Report*, *5*, 95. https://doi.org/10.1007/s40641-019-00127-w

Rio, C., Grandpeix, J. Y., Hourdin, F., Guichard, F., Couvreux, F., Lafore, J. P., & Idelkadi, A. (2013). Control of deep convection by sub-cloud lifting processes: the ALP closure in the LMDZ5B general circulation model. *Climate Dynamics*, *40*, 2271–2292. https://doi.org/10.1007/s00382-012-1506-x

Rio, C., Hourdin, F., Grandpeix, J., & Lafore, J. (2009). Shifting the diurnal cycle of parameterized deep convection over land. *Geophysical Research Letters*, *36*, 7809. https://doi.org/10.1029/2008GL036779

Rochetin, N., Couvreux, F., Grandpeix, J. Y., & Rio, C. (2014a). Deep convection triggering by boundary layer thermals. Part I: LES Analysis and stochastic triggering formulation. *Journal of Atmospheric Sciences*, *71*, 496–514. https://doi.org/10.1175/JAS-D-12-0336.1

Rochetin, N., Grandpeix, J. Y., Rio, C., & Couvreux, F. (2014b). Deep convection triggering by boundary layer thermals. Part II: Stochastic triggering parameterization for the LMDZ GCM. *Journal of Atmospheric Sciences*, *71*, 515–538. https://doi.org/10.1175/JAS-D-12-0337.1

Sadourny, R. (1975). The dynamics of finite-difference models of the shallow-water equations. *Journal of Atmospheric Sciences*, *32*, 680–689.

Sadourny, R., & Laval, K. (1984). January and July performance of the LMD general circulation model. In A. Berger & C. Nicolis (Eds.), *New perspectives in Climate Modeling* (pp. 173–197). Amsterdam: Elsevier.

Sandu, I., Beljaars, A., Bechtold, P., Mauritsen, T., & Balsamo, G. (2013). Why is it so difficult to represent stably stratified conditions in numerical weather prediction (NWP) models? *Journal of Advances in Modeling Earth Systems*, *5*, 117–133. https://doi.org/10.1002/jame.20013

Sandu, I., & Stevens, B. (2011). On the factors modulating the stratocumulus to cumulus transitions. *Journal of Atmospheric Sciences*, *68*, 1865–1881. https://doi.org/10.1175/2011JAS3614.1

Schmidt, G. A., Bader, D., Donner, L. J., Elsaesser, G. S., Golaz, J. C., Hannay, C., & Saha, S. (2017). Practice and philosophy of climate model tuning across six US modeling centers. *Geoscientific Model Development*, *10*(9), 3207–3223. https://doi.org/10.5194/gmd-10-3207-2017

Séférian, R., Baek, S., Boucher, O., Dufresne, J. L., Decharme, B., Saint-Martin, D., & Roehrig, R. (2018). An interactive ocean surface albedo scheme: Formulation and evaluation in two atmospheric models. *Geoscientific Model Development*, *11*, 321–338.

Stan, C., Khairoutdinov, M., DeMott, C. A., Krishnamurthy, V., Straus, D. M., Randall, D. A., & Shukla, J. (2010). An ocean-atmosphere climate simulation with an embedded cloud resolving model. *Geophysical Research Letters*, *37*, L01702. https://doi.org/10.1029/2009GL040822

Stephens, G. L., Li, J., Wild, M., Clayson, C. A., Loeb, N., Kato, S., & Andrews, T. (2012). An update on Earth's energy balance in light of the latest global observations. *Nature Geoscience*, *5*(10), 691–696. https://doi.org/10.1038/ngeo1580

Stouffer, R. J., Eyring, V., Meehl, G. A., Bony, S., Senior, C., Stevens, B., & Taylor, K. E. (2017). CMIP5 scientific gaps and recommendations for CMIP6. *Bulletin of the American Meteorological Society*, *98*(1), 95–105. https://doi.org/10.1175/BAMS-D-15-00013.1

Taylor, K. E., Stouffer, R. J., & Meehl, G. A. (2012). An overview of CMIP5 and the experiment design. *Bulletin of the American Meteorological Society*, *93*, 485–498. https://doi.org/10.1175/BAMS-D-11-00094.1

Thomason, L. W., Ernest, N., Millán, L., Rieger, L., Bourassa, A., Vernier, J. P., & Peter, T. (2018). A global space-based stratospheric aerosol climatology: 1979-2016. *Earth System Science Data*, *10*(1), 469–492. https://doi.org/10.3929/ethz-b-000251695

Turbet, M., Bolmont, E., Leconte, J., Forget, F., Selsis, F., Tobie, G., & Gillon, M. (2018). Modeling climate diversity, tidal dynamics and the fate of volatiles on TRAPPIST-1 planets. *Astronomy and Astrophysics*, *612*, A86. https://doi.org/10.1051/0004-6361/201731620

Vignon, E. (2017). The extreme atmospheric boundary layer over the Antarctic Plateau and its representation in climate models (Unpublished doctoral dissertation), Université Grenoble-Alpes, (Grenoble, France), 275 pp.

Vignon, E., Hourdin, F., Genthon, C., Gallée, H., Bazile, E., Lefebvre, M. P., & Van de Wiel, B. J. H. (2017). Parametrization of the boundary layer over the Antarctic Plateau in a general circulation model: 1D simulations against summertime observations at Dome C. *Journal of Geophysical Research: Atmospheres*, *122*, 6818–6843. https://doi.org/10.1002/2017JD026802

Vignon, E., Hourdin, F., Genthon, C., Van de Wiel, B. J. H., Gallée, H., Madeleine, J. B., & Beaumet, J. (2018). Modeling the dynamics of the atmospheric boundary layer over the Antarctic Plateau with a general circulation model. *Journal of Advance in Modeling Earth Systems*, *10*, 98–125. https://doi.org/10.1002/2017MS001184

Wan, H., Rasch, P. J., Taylor, M. A., & Jablonowski, C. (2015). Short-term time step convergence in a climate model. *Journal of Advance in Modeling Earth Systems*, *7*, 215–225. https://doi.org/10.1002/2014MS000368

Wang, C., Forget, F., Bertrand, T., Spiga, A., Millour, E., & Navarro, T. (2018). Parameterization of rocket dust storms on Mars in the LMD Martian GCM: Modeling details and validation. *Journal of Geophysical Research: Planets*, *123*, 982–1000. https://doi.org/10.1002/2017JE005255

Wang, T., Ottlé, C., Boone, A., Ciais, P., Brun, E., Morin, S., & Peng, S. (2013). Evaluation of an improved intermediate complexity snow scheme in the ORCHIDEE land surface model. *Journal of Geophysical Research: Atmospheres*, *118*, 6064–6079. https://doi.org/10.1002/jgrd.50395

Wei, N., Zhou, L., & Dai, Y. (2017). Evaluation of simulated climatological diurnal temperature range in CMIP5 models from the perspective of planetary boundary layer turbulent mixing. *Climate Dynamics*, *49*, 1–22. https://doi.org/10.1007/s00382-016-3323-0

Williamson, D., Goldstein, M., Allison, L., Blaker, A., Challenor, P., Jackson, L., & Yamazaki, K. (2013). History matching for exploring and reducing climate model parameter space using observations and a large perturbed physics ensemble. *Climate Dynamics*, *41*, 1703–1729. https://doi.org/10.1007/s00382-013-1896-4

Yamada, T. (1983). Simulations of nocturnal drainage flows by a q^2l turbulence closure model. *Journal of the Atmospheric Sciences*, *40*, 91–106.